Improved bounds on the heavy neutrino productions at the LHC

Arindam Das[1] and Nobuchika Okada[2]

Department of Physics and Astronomy, University of Alabama, Tuscaloosa, Alabama 35487, USA

arXiv:1510.04790v2 [hep-ph] 29 Oct 2015

Abstract

The Majorana neutrino in type-I seesaw and the pseudo-Dirac neutrinos in the inverse seesaw can have sizable mixings with the light neutrinos in the standard model (SM), through which the heavy neutrinos can be produced at the Large Hadron Collider (LHC). In producing the heavy neutrinos we study a variety of initial states such as quark-quark, quark-gluon and gluon-gluon as well as photon mediated processes. For the Majorana heavy neutrino production we consider same-sign di-lepton plus di-jet as the signal events. Using the recent ATLAS and CMS data at $\sqrt{s} = 8$ TeV with 20.3 fb^{-1} and 19.7 fb^{-1} luminosities, respectively, we obtain direct upper bounds on the light-heavy neutrino mixing angles. For the pseudo-Dirac heavy neutrino production we consider the final sate with tri-lepton plus missing energy as the signal events. Using the recent anomalous multi-lepton search by CMS at $\sqrt{s} = 8$ TeV with 19.5 fb^{-1} luminosity we obtain upper bounds on the mixing angles. Taking the varieties of initial states into account, the previously obtained upper bounds on the mixing angles have been improved. We scale our results at the 8 TeV LHC to obtain a prospective search reach at the 14 TeV LHC with high luminosities.

[1]adas8@ua.edu
[2]okadan@ua.edu

1. Introduction

The current neutrino oscillation data [1]-[6] have established the existence of the neutrino mass and the flavor mixing. This requires us to extend the Standard Model (SM). The seesaw extension [7]-[11] of the SM is probably the simplest idea which can naturally explain the tiny neutrino mass. In case of type-I seesaw, the SM is extended by introducing SM-singlet heavy Majorana neutrino which induce a dimension five operator, leading to a very small light Majorana neutrino masses. If such heavy neutrino mass lies in the electroweak scale, then the heavy neutrinos can be produced in the high energy colliders such as the Large Hadron Collider (LHC) and International Linear Collider (ILC) [12, 13]. As the heavy neutrinos are singlet under the SM gauge group, they obtain the couplings with the SM gauge bosons only through the mixing with light SM neutrinos via the Dirac Yukawa coupling. In the general parameterization for the seesaw formula [14], the Dirac Yukawa coupling can be sizable for the electroweak scale heavy neutrinos, while reproducing the neutrino oscillation data.

There is another kind of seesaw mechanism, so-called inverse seesaw [15, 16], where the small Majorana neutrino mass originates from tiny lepton number violating parameters, rather than the suppression by the heavy neutrino mass in the conventional seesaw mechanism. In this case the heavy neutrinos are pseudo-Dirac particles and their Dirac Yukawa couplings can be even order one, while reproducing the tiny neutrino mass. Thus, at the high energy colliders the heavy pseudo-Dirac neutrino can be produced through a sizable mixing with the SM neutrinos.

In this paper we study the heavy neutrino production at the LHC through a variety of initial states such as quark-quark $\left(q\overline{q'}\right)$, quark-gluon (qg) and gluon-gluon (gg) as well as the photon mediated processes. For fixed heavy neutrino masses (m_N) we calculate the individual cross section of the respective processes normalized by the square of the mixing angles between light and the heavy neutrinos. We also study the kinematic distributions of the signal events produced by different initial states and find the characteristic distributions corresponding to the individual initial states.

For the Majorana heavy neutrino case we consider the same sign di-lepton plus two jet signal. Using the recent collider studies [17]-[19] we put an upper limit on the light-heavy mixing angles. For the pseudo-Dirac heavy neutrino we consider tri-lepton plus missing energy signal. We compare the upper bounds with those obtained by other experiments [20]-[25]. Though some updated analysis could be found in [26, 27] Using all the initial states the upper bounds given in [28] are improved.

This paper is organized as follows. In Sec. 2, we introduce the models for the type-I and the inverse seesaws. We calculate the production cross sections of the heavy neutrinos at the LHC with a variety of initial states in Sec 3. In Sec. 4, we study the kinematic distributions of the final

state particles associated with the heavy neutrino productions for the individual initial states. In Sec. 5 we simulate the signal events for the heavy neutrino productions. Comparing the generated events with the current LHC data, we obtain improved upper bounds on the mixing angles between the light-heavy neutrinos for the type-I and inverse seesaws, respectively. Sec. 6 is devoted for conclusions.

2. The Models

In type-I seesaw [29, 30], we introduce SM gauge-singlet right handed Majorana neutrinos N_R^β, where β is the flavor index. N_R^β couple with SM lepton doublets ℓ_L^α and the SM Higgs doublet H. The relevant part of the Lagrangian is

$$\mathcal{L} \supset -Y_D^{\alpha\beta}\overline{\ell_L^\alpha} H N_R^\beta - \frac{1}{2} m_N^{\alpha\beta}\overline{N_R^{\alpha C}} N_R^\beta + H.c.. \tag{1}$$

After the spontaneous electroweak symmetry breaking by the vacuum expectation value (VEV), $H = \begin{pmatrix} \frac{v}{\sqrt{2}} \\ 0 \end{pmatrix}$, we obtain the Dirac mass matrix as $M_D = \frac{Y_D v}{\sqrt{2}}$. Using the Dirac and Majorana mass matrices we can write the neutrino mass matrix as

$$M_\nu = \begin{pmatrix} 0 & M_D \\ M_D^T & m_N \end{pmatrix}. \tag{2}$$

Diagonalizing this matrix we obtain the seesaw formula for the light Majorana neutrinos as

$$m_\nu \simeq -M_D m_N^{-1} M_D^T. \tag{3}$$

For $m_N \sim 100$ GeV, we may find $Y_D \sim 10^{-6}$ with $m_\nu \sim 0.1$ eV. However, in the general parameterization for the seesaw formula [14], Y_D can be as large as 1, and this is the case we consider in this paper.

There is another seesaw mechanism, so-called inverse seesaw [15, 16], where the light Majorana neutrino mass is generated through tiny lepton number violation. The relevant part of the Lagrangian is given by

$$\mathcal{L} \supset -Y_D^{\alpha\beta}\overline{\ell_L^\alpha} H N_R^\beta - m_N^{\alpha\beta}\overline{S_L^\alpha} N_R^\beta - \frac{1}{2}\mu_{\alpha\beta}\overline{S_L^\alpha} S_L^{\beta C} + H.c., \tag{4}$$

where N_R^α and S_L^β are two SM-singlet heavy neutrinos with the same lepton numbers, m_N is the Dirac mass matrix, and μ is a small Majorana mass matrix violating the lepton numbers. After the electroweak symmetry breaking we obtain the neutrino mass matrix as

$$M_\nu = \begin{pmatrix} 0 & M_D & 0 \\ M_D^T & 0 & m_N^T \\ 0 & m_N & \mu \end{pmatrix}. \tag{5}$$

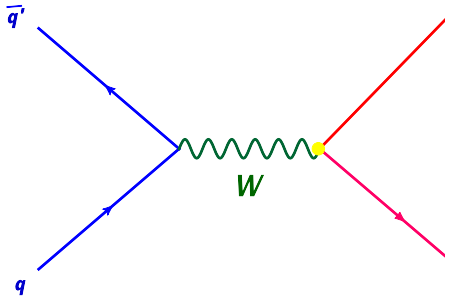

Figure 1: Feynman diagram for $N\ell$ production from the $q\overline{q'}$ annihilation.

Diagonalizing this mass matrix we obtain the light neutrino mass matrix

$$M_\nu \simeq M_D m_N^{-1} \mu m_N^{-1^T} M_D^T. \tag{6}$$

Note that the smallness of the light neutrino mass originates from the small lepton number violating term μ. The smallness of μ allows the $m_D m_N^{-1}$ parameter to be order one even for an electroweak scale heavy neutrino. Since the scale of μ is much smaller than the scale of m_N, the heavy neutrinos become the pseudo-Dirac particles. This is the main difference between the type-I and the inverse seesaws. See, for example, [31] for the interaction Lagrangians and the partial decay widths of the heavy neutrinos.

3. Heavy neutrino production at the LHC

We implement our model in the generator `MadGraph5-aMC@NLO` [32]-[34] and calculate the production cross section of the heavy neutrino with a variety of initial states such as $q\overline{q'}$, qg and gg as well as photon mediated processes. For the final states we consider $N\ell + n-$jet, where the number of jets is $n = 0, 1, 2$. We separately calculate the production cross sections for individual initial states to understand which initial states dominantly contribute to the production process of the heavy neutrino. See [35]-[64]for recent studies on heavy neutrino production at high energy colliders.

3.1. $N\ell$ and $N\ell j$ production processes from $q\overline{q'}$ and qg initial states

We first consider the final state $N\ell$ from $q\overline{q'}$, and $N\ell j$ from both of $q\overline{q'}$ and qg initial states. The relevant Feynman diagrams with the initial $q\overline{q'}$ state are shown in Figs. 1 and 2, while those with the initial qg state are shown in Fig. 3. Fig. 4 shows the combined heavy neutrino production cross section normalized by the square of the mixing angle from the two initial states. For the final state $N\ell j$ we impose the minimum transverse momentum of the jet (p_T^j) as 10 GeV, 20 GeV and 30 GeV, respectively. In generating the events we set the `Xqcut`$= p_T^j$

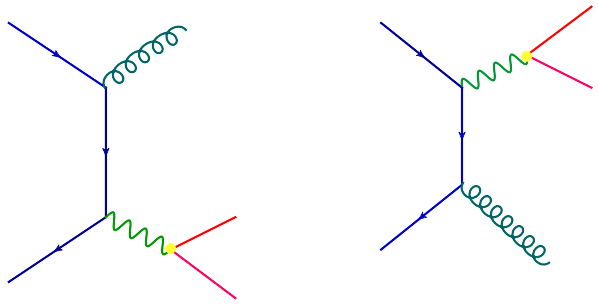

Figure 2: Feynman diagrams for $N\ell j$ production from the $q\overline{q'}$ annihilation.

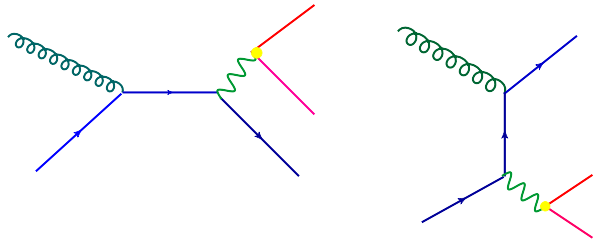

Figure 3: Feynman diagrams for $N\ell j$ production from the qg fusion.

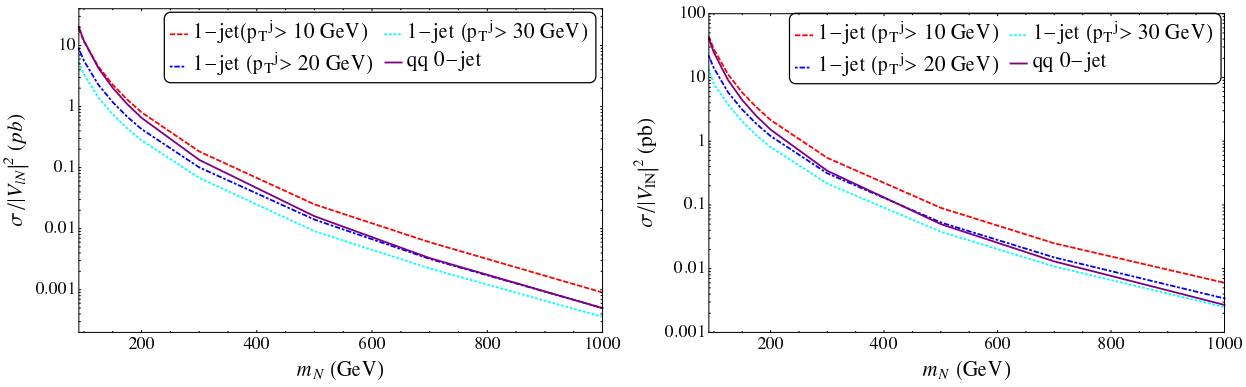

Figure 4: The left panel shows the cross sections as a function of m_N normalized by the square of the mixing angle for the $N\ell j$ final state at the $p_T^j > 10$ GeV (dashed), $p_T^j >$20 GeV (dot-dashed) and $p_T^j > 30$ GeV (dotted) from the $q\overline{q'}$ and qg initial states and the $N\ell$ final state from the qq initial states (solid) at the 8 TeV LHC. The right panel is same as the left panel but at the 14 TeV LHC.

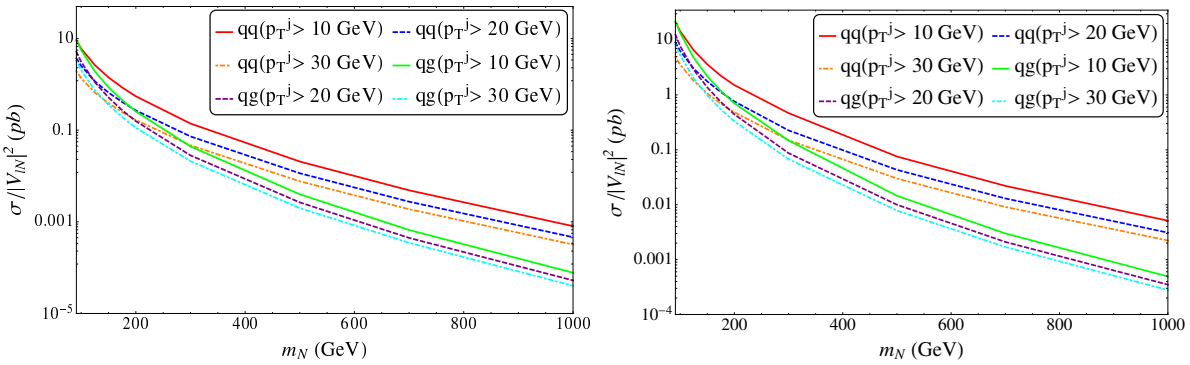

Figure 5: The decomposition of the cross section for the individual initial states for different p_T^j cuts such that $p_T^j > 10$ GeV (solid), $p_T^j > 20$ GeV (dashed) and $p_T^j > 30$ GeV (dot-dashed). The cross sections at the 8 TeV LHC are shown in the left panel where as those at the 14 TeV LHC are shown in the right panel.

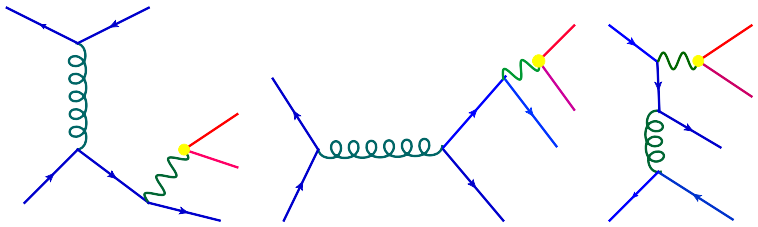

Figure 6: Sample Feynman diagrams for $N\ell jj$ production processes from the $q\overline{q'}$ initial state.

in MadGraph with the `MLM` matching scheme (`ickkw`= 1) [65]- [69]. The left panel shows the results for $\sqrt{s}$ =8 TeV, while $\sqrt{s}$ =14 TeV LHC results are shown in the right panel. The $N\ell j$ cross section dominates over the production, while for a higher p_T^j cut the $N\ell$ cross section dominates.

We show in Fig. 5 the decomposition of the cross sections shown in Fig. 4 for individual final states. The left panel shows the results for $\sqrt{s}$ =8 TeV, while $\sqrt{s}$ =14 TeV results are shown in the right panel. The cross section from the $q\overline{q'}$ initial state dominates over the one from the qg initial state for the cut of $p_T^j > 10$ GeV. With the increase of the p_T^j cut the cross section from the qg initial state becomes dominant for the small mass region of the heavy neutrino, as pointed out in [28]. This is because the parton distribution function (PDF) of gluon is much larger than the PDFs of quarks at the low Bjorken scaling parameter. As the heavy neutrino mass becomes larger, the cross section from $q\overline{q'}$ takes over the one from qg because the gluon PDF sharply drops toward the high Bjorken scaling parameter.

3.2. $N\ell jj$ production processes from $q\overline{q'}$, qg and gg initial states

Next we consider the $N\ell jj$ final state which comes from the $q\overline{q'}$, qg and gg initial states. The relevant Feynman diagrams with the initial $q\overline{q'}$, qg and gg states are shown in Figs. 6-8.

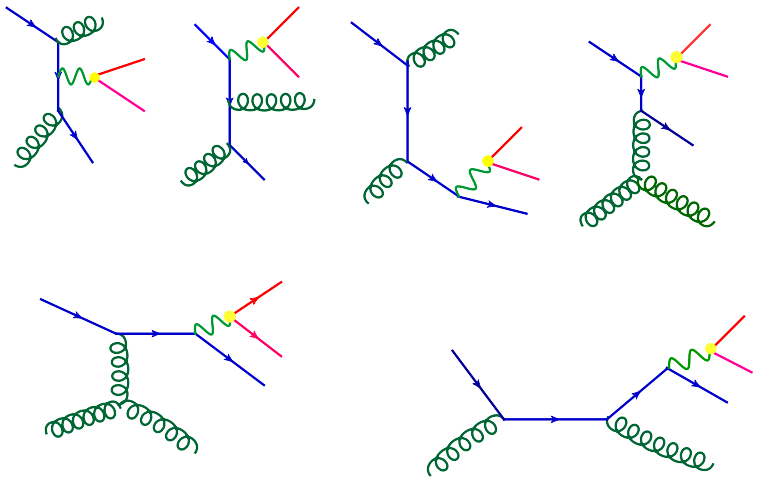

Figure 7: Sample Feynman diagrams for $N\ell jj$ production processes from the qg fusion.

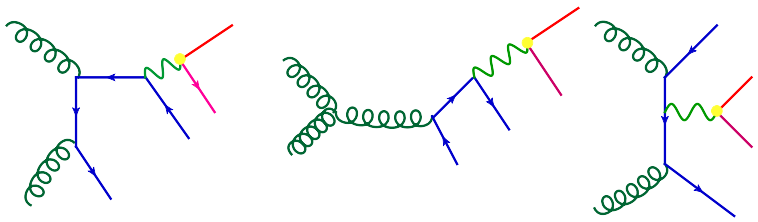

Figure 8: Sample Feynman diagrams for $N\ell jj$ production processes from the gg fusion.

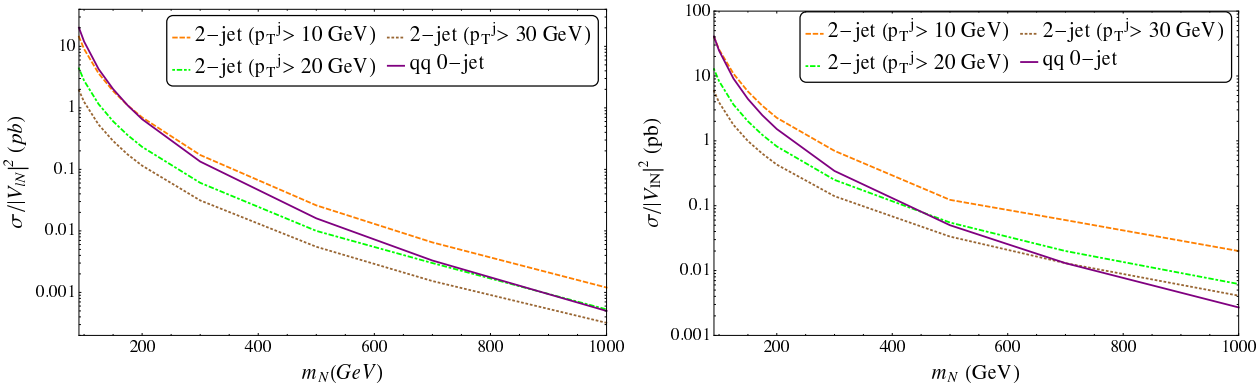

Figure 9: The left panel shows the cross sections as a function of m_N normalized by the square of the mixing angle for the $N\ell jj$ final state for $p_T^j > 10$ GeV (dashed), $p_T^j >$20 GeV (dot-dashed) and $p_T^j > 30$ GeV (dotted) from the $q\overline{q'}$, qg and gg initial states and the $N\ell$ final state from the $q\overline{q'}$ initial state (solid) at the 8 TeV LHC. The right panel shows the results for the 14 TeV LHC.

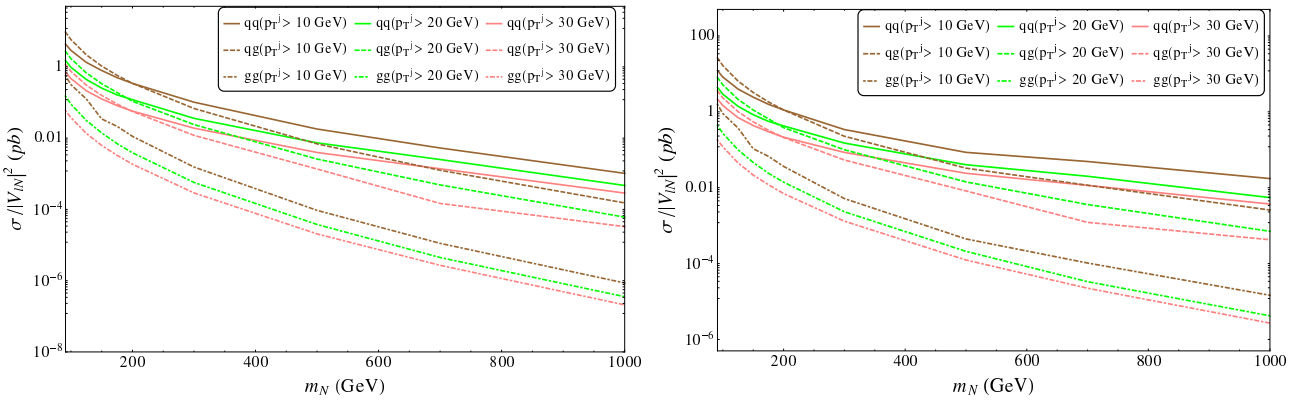

Figure 10: The decomposition of the cross section for the individual initial states for different p_T^j cuts such that $p_T^j > 10$ GeV (solid), $p_T^j > 20$ GeV (dashed) and $p_T^j > 30$ GeV (dot-dashed). The cross sections at the 8 TeV are shown in the left panel where as those at the 14 TeV are shown in the right panel.

Fig. 9 shows the combined heavy neutrino production cross section normalized by the square of the mixing angle from the three initial states. For the final state $N\ell jj$ we impose the minimum transverse momentum for each jet (p_T^j) as 10 GeV, 20 GeV and 30 GeV, respectively. As in the previous sub-section we set the `Xqcut`= p_T^j in MadGraph with the `MLM` matching scheme. The left panel shows the results for $\sqrt{s}$ =8 TeV, while those for $\sqrt{s}$ =14 TeV are shown in the right panel. The $N\ell jj$ cross section dominates over the production cross section for the final state with zero jet for the 10 GeV p_T^j cut, while for a higher p_T^j cut the $N\ell$ cross section dominates.

We show in Fig. 10 the decomposition of the cross sections shown in Fig. 9 for individual initial states. The left panel shows the results for $\sqrt{s}$ =8 TeV, while results for $\sqrt{s}$ =14 TeV are shown in the right panel. The cross section from the $q\overline{q'}$ initial state dominates over those from the qg and gg initial states for the cut of $p_T^j > 10$ GeV when $m_N \gtrsim 200$ GeV, while for $m_N \lesssim 200$ GeV the qg initial state dominates. This is in contrast with the results for the $N\ell j$, where $q\overline{q'}$ initial state always dominates the cross section. Although we may think that the gluon fusion channel could dominate, it is found to be always smaller than the other channels. This is because the Bjorken scaling parameters for two gluons can not be small simultaneously in order to produce the heavy neutrino. On the other hand, we expect the gluon fusion channel cross section becomes larger as we lower the heavy neutrino mass. We can see in Fig. 10 the gluon fusion channel rises sharper than the others towards the low mass region. We see that as the heavy neutrino mass becomes larger, the cross section from $q\overline{q'}$ takes over those from the qg and gg because the gluon PDF sharply drops towards the high Bjorken scaling parameter.

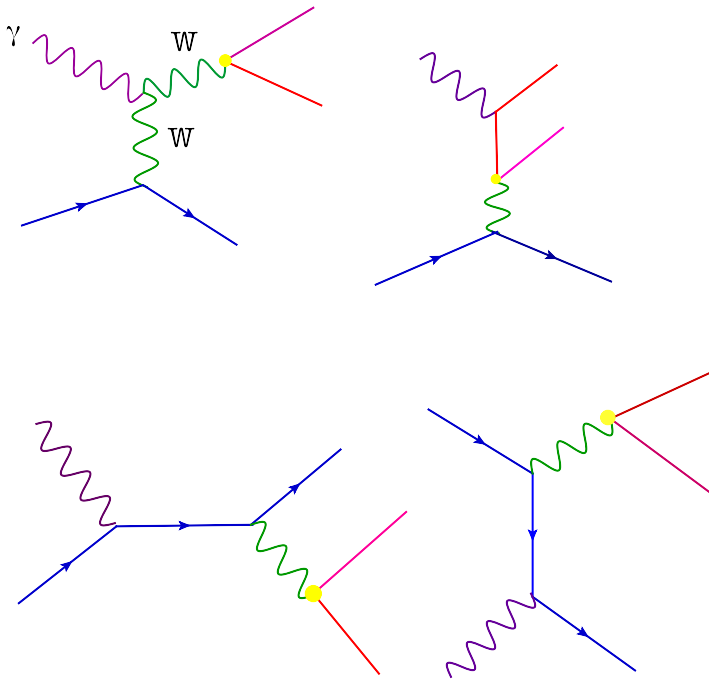

Figure 11: The elastic or inelastic process for the $N\ell j$ final state.

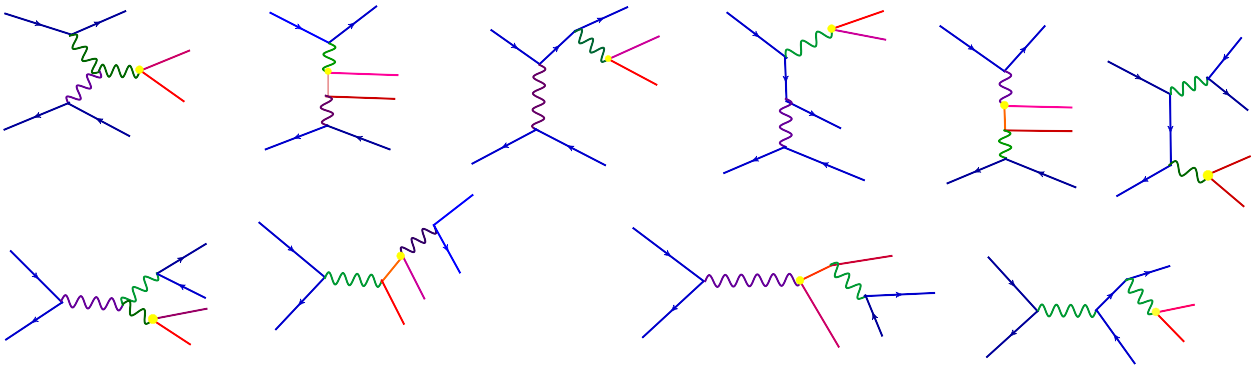

Figure 12: The deep-inelastic processes for the $N\ell jj$ final state mediated by photon.

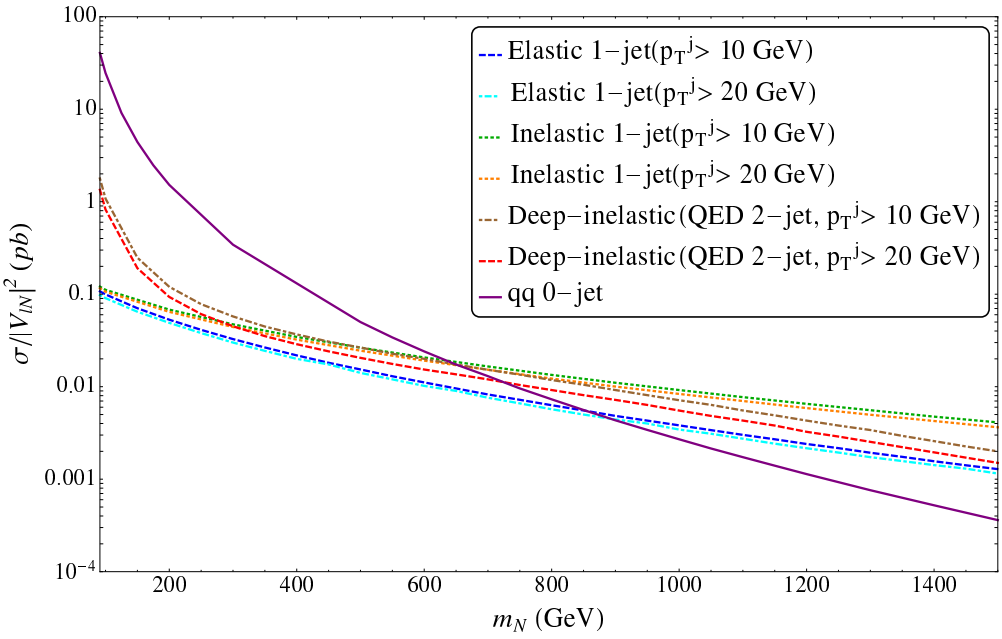

Figure 13: Figure shows the production cross section of the heavy neutrino as a function of m_N and normalized by the square of the mixing angle for the different photon mediated processes at the 14 TeV LHC. The solid line stands for the $N\ell$ final state for the $q\overline{q'}$ initial state. The elastic process for different p_T^j values are shown by the dashed lines. The inelastic processes are represented by the dotted lines. The deep inelastic process (QED 2-jet) is depicted by the dot-dashed lines.

3.3. $N\ell j$ and $N\ell jj$ production processes from photon mediated processes

Apart from the QCD processes we also consider the heavy neutrino production at the LHC through the photon mediated processes. There are three types of photon mediated processes. The first one is the elastic process where one photon is radiated from one proton and then scatters with a parton in the other proton. The second one is the inelastic process where one photon is radiated from a parton inside one proton and scatters with a parton inside the other proton (for relevant Feynman diagrams, see Fig. 11). The third one is the deep-inelastic scattering mediated by photon with a large momentum transfer. (See Fig. 12 for relevant Feynman diagrams.) Analysis of the deep inelastic process has been performed in [70]. All of these processes have been analyzed in [71].

We calculate the heavy neutrino production cross sections through the three photon mediated processes. For the deep-inelastic processes we switch off the QCD vertices in `MadGraph`. Our results are shown in Fig. 13 for $\sqrt{s} = 14$ TeV LHC. Here we have imposed two different values of the p_T^j cuts, $p_T^j > 10$ GeV and 20 GeV. When $m_N \lesssim 400$ (300) GeV, the deep-inelastic process dominates over the other photon mediated processes for $p_T^j > 10$ (20) GeV and otherwise, the inelastic process dominates. The elastic process is always small compared to the

others. The analytic expressions of the radiated photon PDFs used in our calculations are given in [72]-[80].

4. Kinematic distributions of the heavy neutrino production

Here we investigate the kinematic distributions of the leptons and jets associated with the heavy neutrino production. The different production processes show typical kinematic distributions. To see this we generate the events for $m_N = 100$ GeV and 500 GeV at the $\sqrt{s} = 14$ TeV LHC. We consider the transverse momenta (p_T) and pseudo-rapidities (η) for the leptons, jets and the heavy neutrino as kinematic variables. We also consider the differential cross sections for the final states of $N\ell$, $N\ell j$ and $N\ell jj$ with the cut $p_T^j > 20$ GeV for the process/es with jet(s).

The kinematics distributions for the final state $N\ell$ are shown in Fig. 14. The $\eta^{\ell,N}$ distributions show peaks around $\eta = 0$ and become sharper with the increase in m_N. The invariant mass distribution shows a sharp peak in the vicinity of the heavy neutrino mass threshold, which means most of the particles are produced almost at rest. For the final state $N\ell j$, the kinetic distributions are shown in Figs. 15 and 16. These distributions show similar behaviors to the results for the $N\ell$ final state. Same for the final state $N\ell jj$ are shown in Figs. 17-19. In Fig. 18 the leading jet is defined as j_2 while the j_1 is the non-leading jet ($p_T^{j_2} > p_T^{j_1}$ for each event). The $\eta^{j_{1,2}}$ distributions are flatter than those in the $N\ell j$ case. This is because many events include the radiated jets.

We also show the kinematic distributions from the photon mediated processes for the final states $N\ell j$ and $N\ell jj$. The $N\ell j$ final state comes from the elastic and inelastic processes whereas the $N\ell jj$ comes from the deep inelastic process. Figs. 20 and 21 show the kinematic distributions for the elastic process. Corresponding results for the inelastic process are shown in Figs. 22 and 23. Finally the results for the deep inelastic processes are shown in Figs 24-26. The $\eta^{j_{1,2}}$ distributions show the double peaks in all three cases which is a typical feature of the photon mediated processes [71].

5. Data analysis and the upper bounds for the mixing angles

The signal events at the parton level were generated by `MadGraph5`. The showering and hadronization of the events were performed with `PYTHIA6.4` [81] and a fast detector simulation was done using `DELPHES3` [82, 83] bundled with `MadGraph`. Hadrons were clustered into jets using the anti-k_T algorithm as implemented in `FastJet2` [84, 85] with a distance parameter of 0.5. As our signal events are accompanied by n-jets, we incorporate the `MLM` matching prescription according to [65]-[69] to avoid the double counting of jets and use the matched

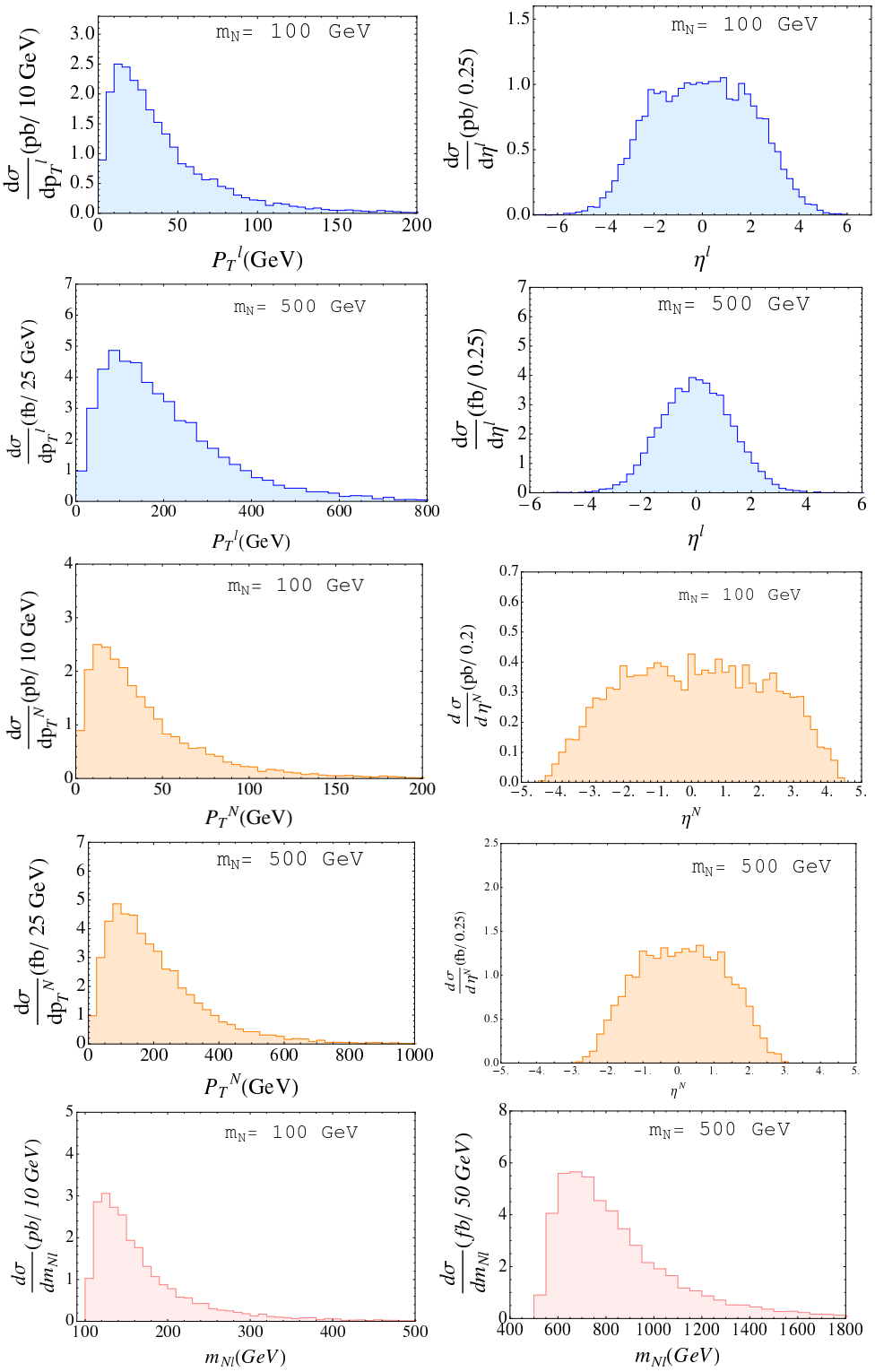

Figure 14: The first and second rows show the p_T and η distributions of the lepton produced in the $N\ell$ final state from the $q\overline{q'}$ 0-jet processes. The third and fourth rows show the same for the heavy neutrino. The fifth row shows the final state invariant mass ($m_{N\ell}$) distributions. The left column stands for $m_N = 100$ GeV whereas the right one is for $m_N = 500$ GeV.

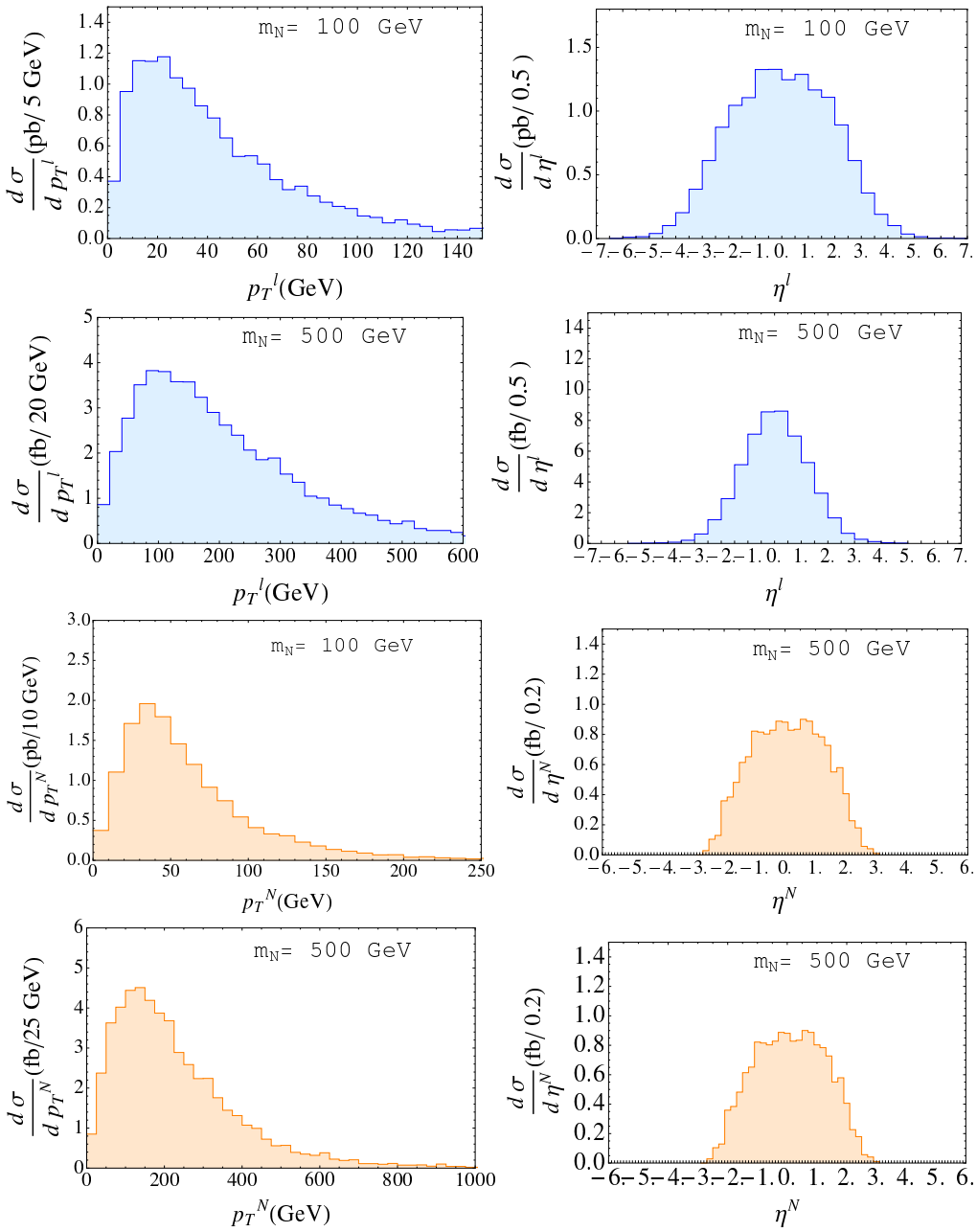

Figure 15: The first and second rows show the p_T and η distributions of the lepton produced in the $N\ell j$ final state from the $q\overline{q'}$ and qg 1-jet processes. The third and fourth rows show the same for the heavy neutrino. The left column stands for $m_N = 100$ GeV whereas the right one is for $m_N = 500$ GeV.

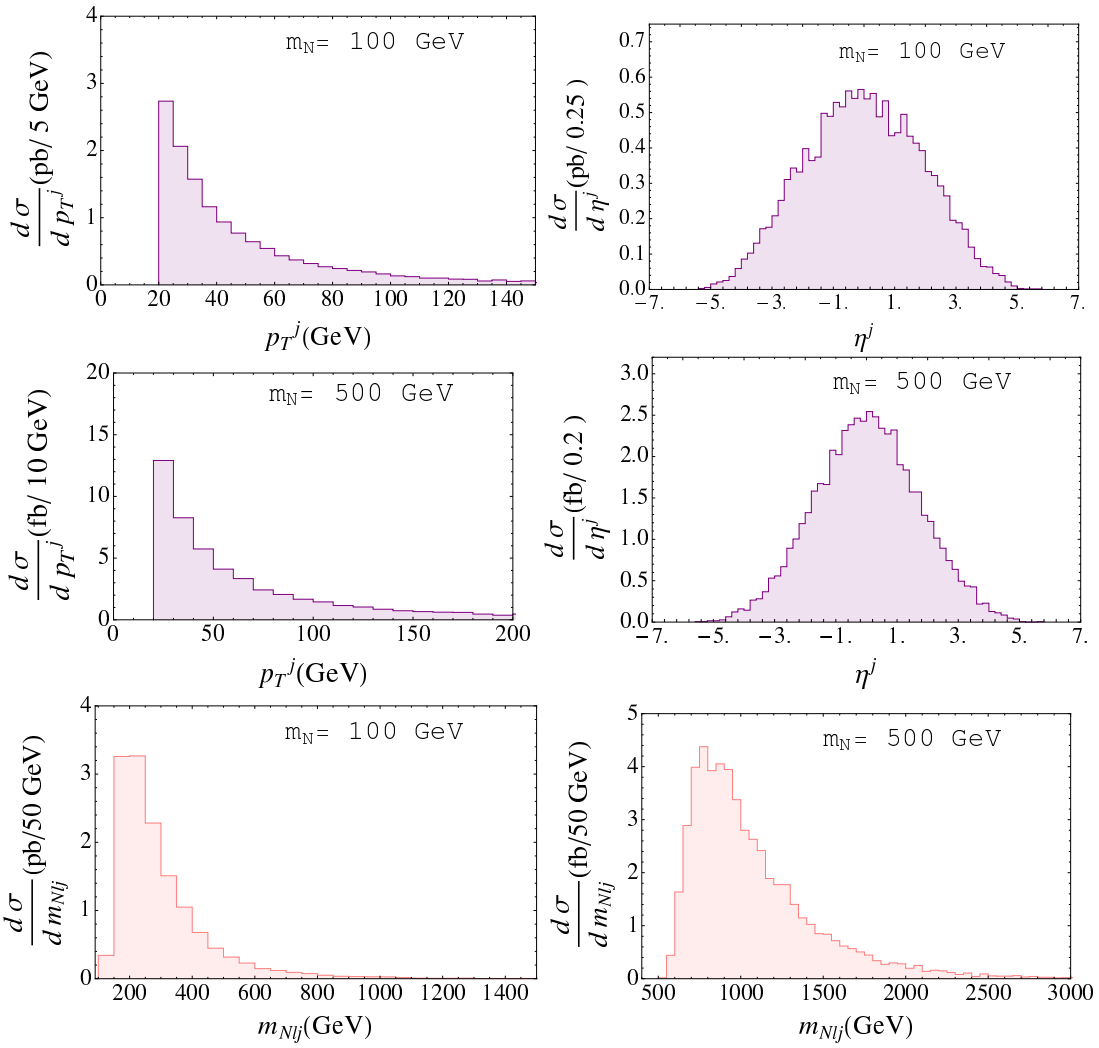

Figure 16: The first and second rows show the p_T and η distributions of the jet produced in the $N\ell j$ final state from the $q\bar{q}'$ and qg 1-jet processes. The third row shows the final state invariant mass ($m_{N\ell j}$) distributions. The left column stands for $m_N = 100$ GeV whereas the right one is for $m_N = 500$ GeV.

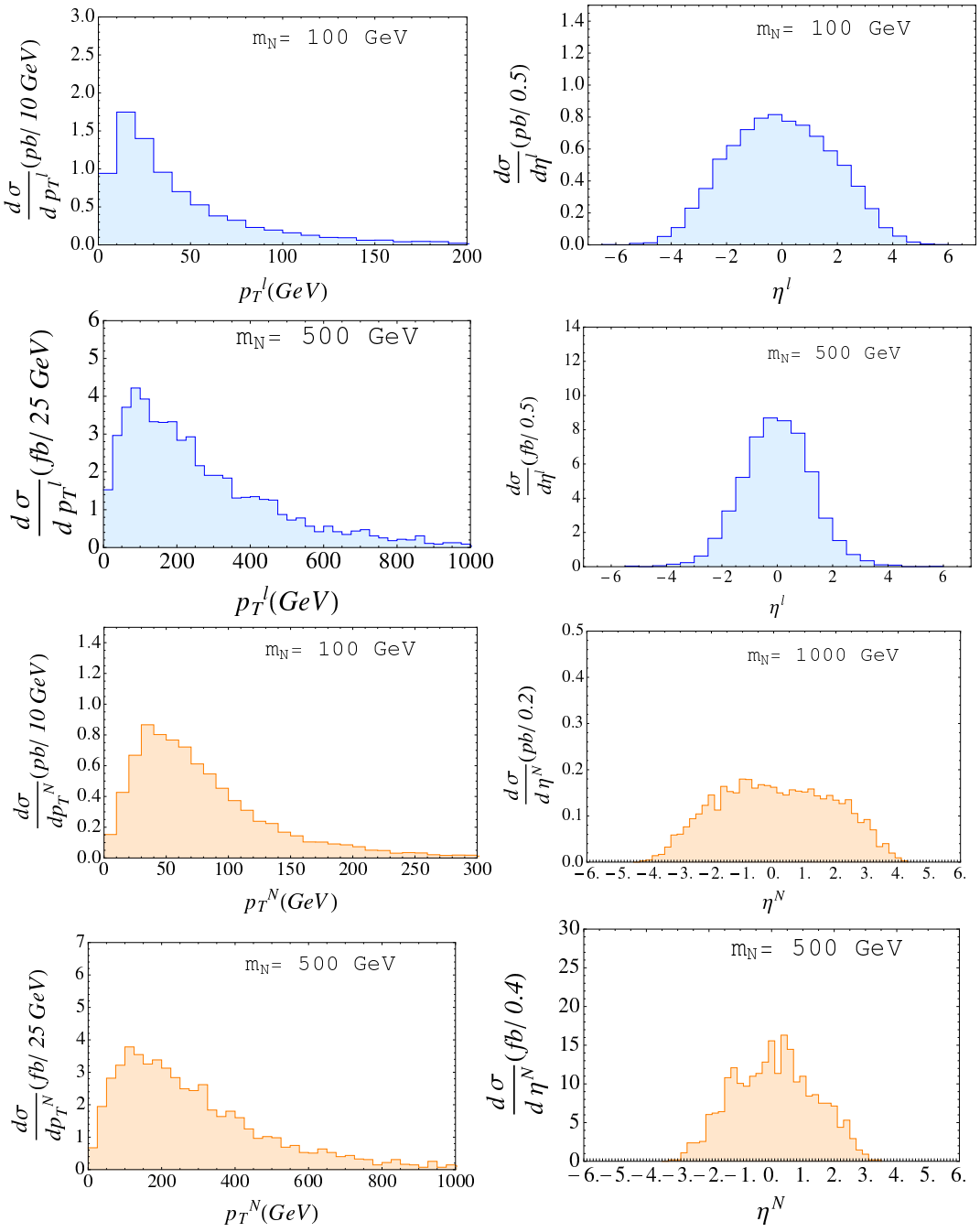

Figure 17: The first and second rows show the p_T and η distributions of the lepton produced in the $N\ell jj$ final state from the $q\overline{q'}$, qg and gg initial states. The third and fourth rows show the same for the heavy neutrino. The left column stands for $m_N = 100$ GeV whereas the right one is for $m_N = 500$ GeV.

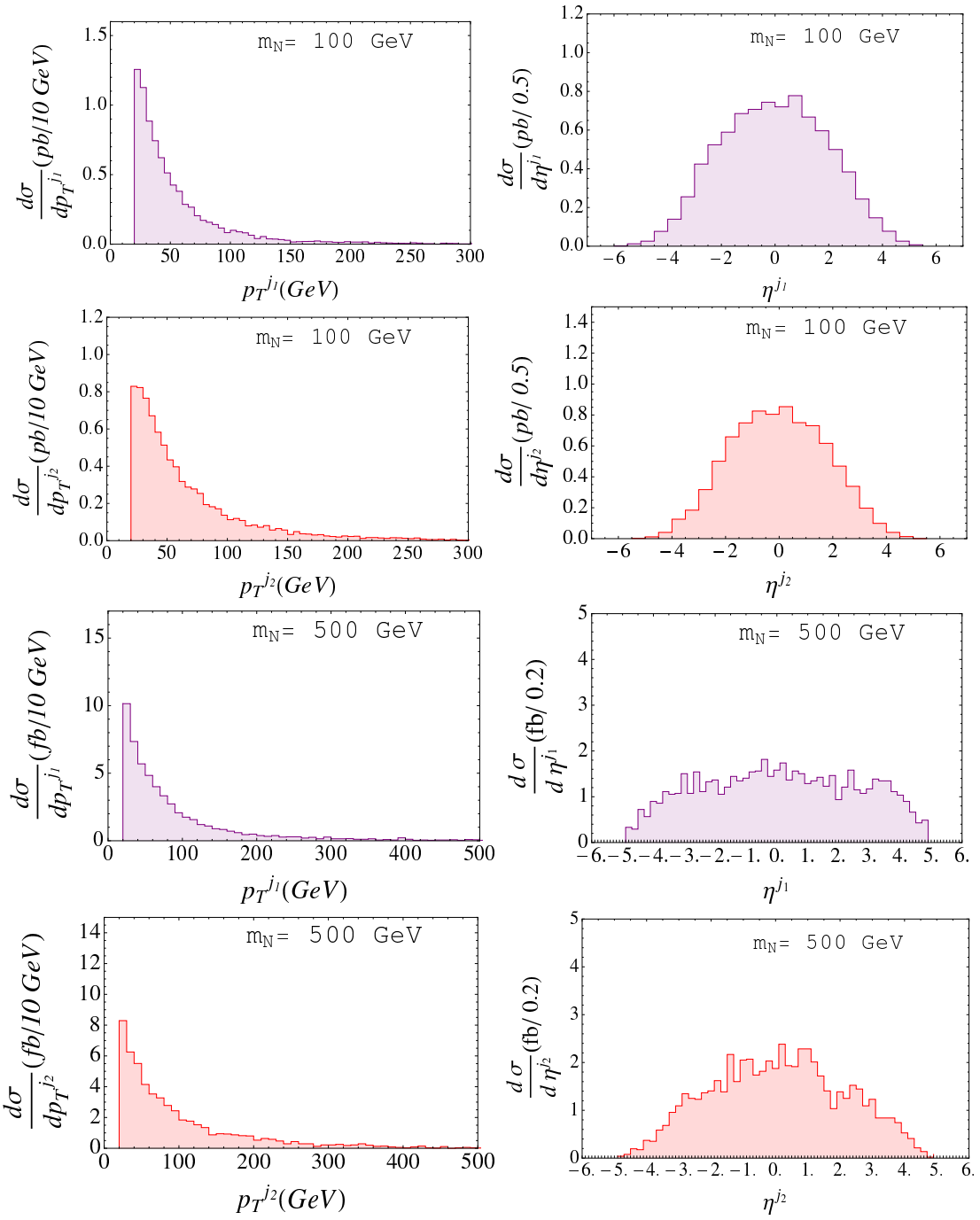

Figure 18: The first and second rows show the p_T and η distributions of the non-leading jet produced in the $N\ell jj$ final state from the $q\overline{q'}$, qg and gg initial states. The third and fourth rows show the same for the leading jet. The left column stands for $m_N = 100$ GeV whereas the right one is for $m_N = 500$ GeV.

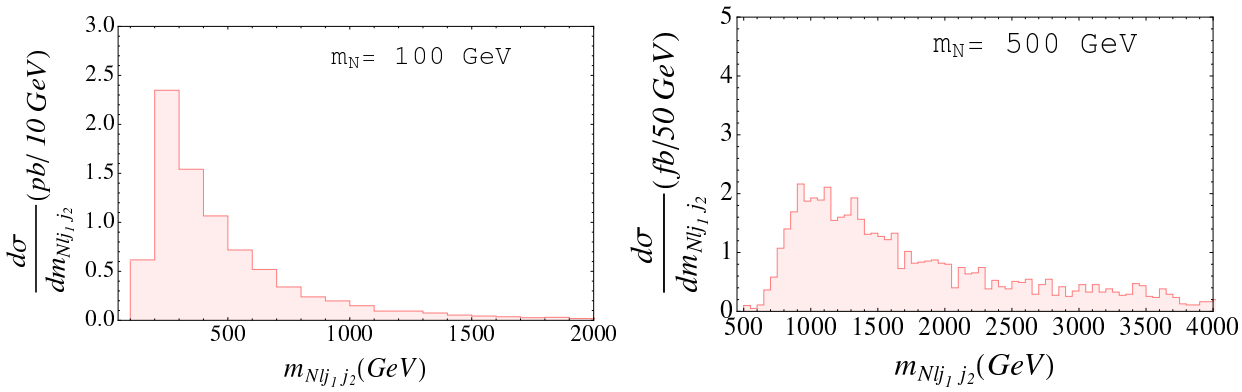

Figure 19: The final state invariant mass ($m_{N\ell j_1 j_2}$) distributions produced in the $N\ell jj$ final state from the $q\overline{q'}$, qg and gg initial states. The left panel shows $m_N = 100$ GeV whereas the right one shows $m_N = 500$ GeV.

cross section and events for the analysis after the detector simulation. We consider two cases for the types of heavy neutrinos. One is the Majorana case for which the signal process is $pp \to N\ell_1^\pm / N\ell_1^\pm j / N\ell_1^\pm jj$, followed by $N \to \ell_2^\pm W^\mp$ and $W^\mp \to jj$. The other is the pseudo-Dirac case for which the signal process is $pp \to N\ell_1^+ / N\ell_1^+ j / Nl_1^+ jj$, followed by $N \to \ell_2^- W^+$ and $W^+ \to \ell_3^+ \nu$ ($pp \to \overline{N}\ell_1^- / \overline{N}\ell_1^- j / \overline{N}\ell_1^- jj$, followed by $\overline{N} \to \ell_2^+ W^-$ and $W^- \to \ell_3^- \overline{\nu}$).

5.1. Same-sign di-lepton plus di-jet signal

For simplicity we consider the case that only one generation of the heavy neutrino is light and accessible to the LHC which couples to only the second generation of the lepton flavor. To generate the events in the `MadGraph` we use the `NN23LO1 PDF` [86]-[89] with `Xqcut`= $p_T^j = 20$ GeV and `QCUT`= 25 GeV. We calculate the cross sections for the processes $\sigma_{0-j} = \sigma(pp \to N\mu^\pm \to \mu^\pm\mu^\pm jj)$, $\sigma_{1-j} = \sigma(pp \to N\mu^\pm j \to \mu^\pm j\mu^\pm jj)$ and $\sigma_{2-j} = \sigma(pp \to N\mu^\pm jj \to \mu^\pm jj\mu^\pm jj)$ as functions of m_N. Comparing our generated events with the recent ATLAS results [18] at the 8 TeV LHC with the luminosity 20.3 fb^{-1}, we obtain an upper limit on the mixing angles between the Majorana type heavy neutrino and the SM leptons as a function of m_N. In the ATLAS analysis the upper bound of the production cross section (σ^{ATLAS}) is obtained for the final state with the same-sign di-muon plus di-jet as a function of m_N. Using these cross sections we obtain the upper bounds on the mixing angles as follows

$$|V_{\ell N}|^2_{0-j} \lesssim \frac{\sigma^{ATLAS}}{\sigma_{0-j}}, \tag{7}$$

$$|V_{\ell N}|^2_{1-j} \lesssim \frac{\sigma^{ATLAS}}{\sigma_{0-j} + \sigma_{1-j}}, \tag{8}$$

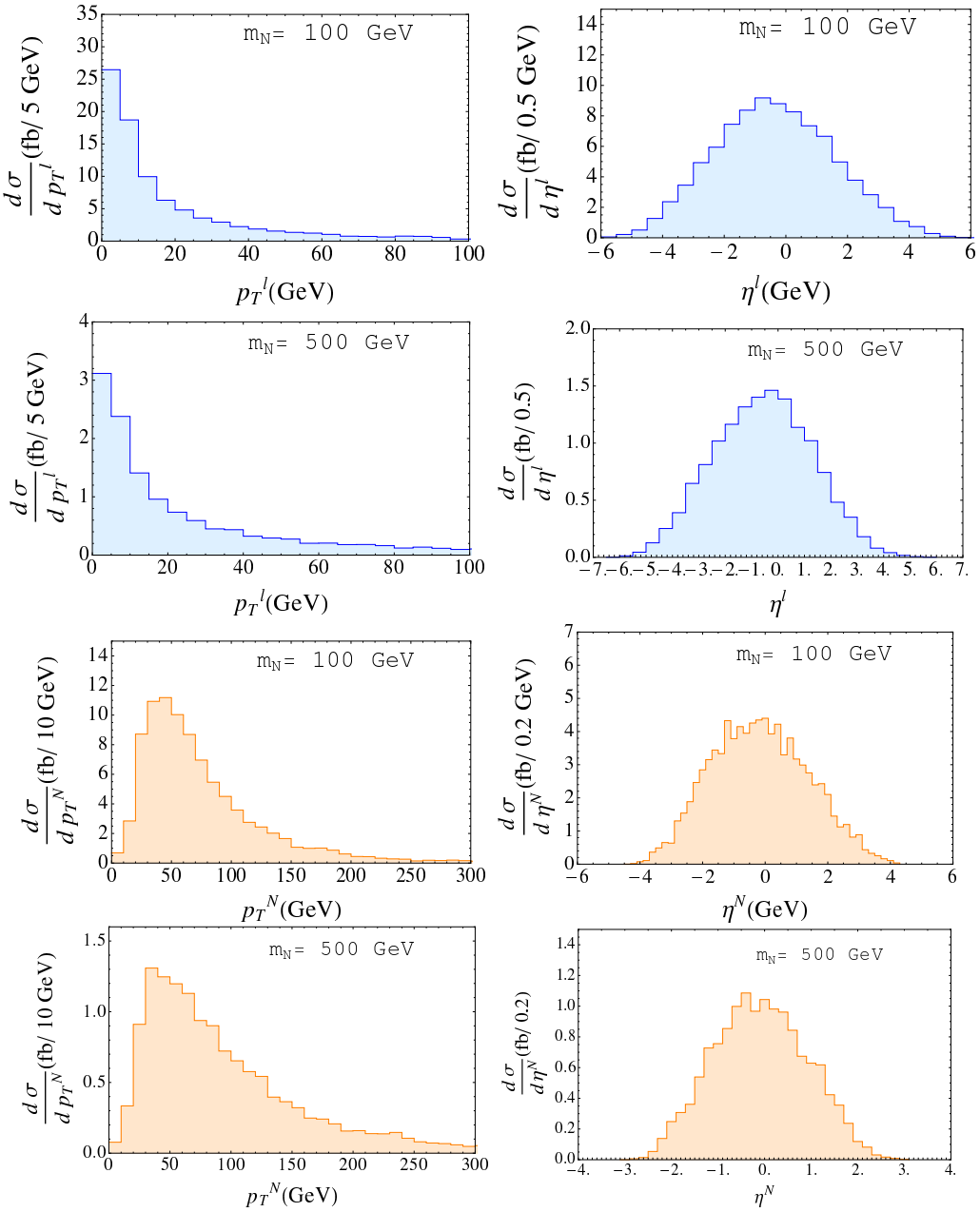

Figure 20: The first and second rows show the p_T and η distributions of the lepton produced in the $N\ell j$ final state from the photon mediated elastic processes. The third and fourth rows show the same for the heavy neutrino. The left column stands for $m_N = 100$ GeV whereas the right one is for $m_N = 500$ GeV.

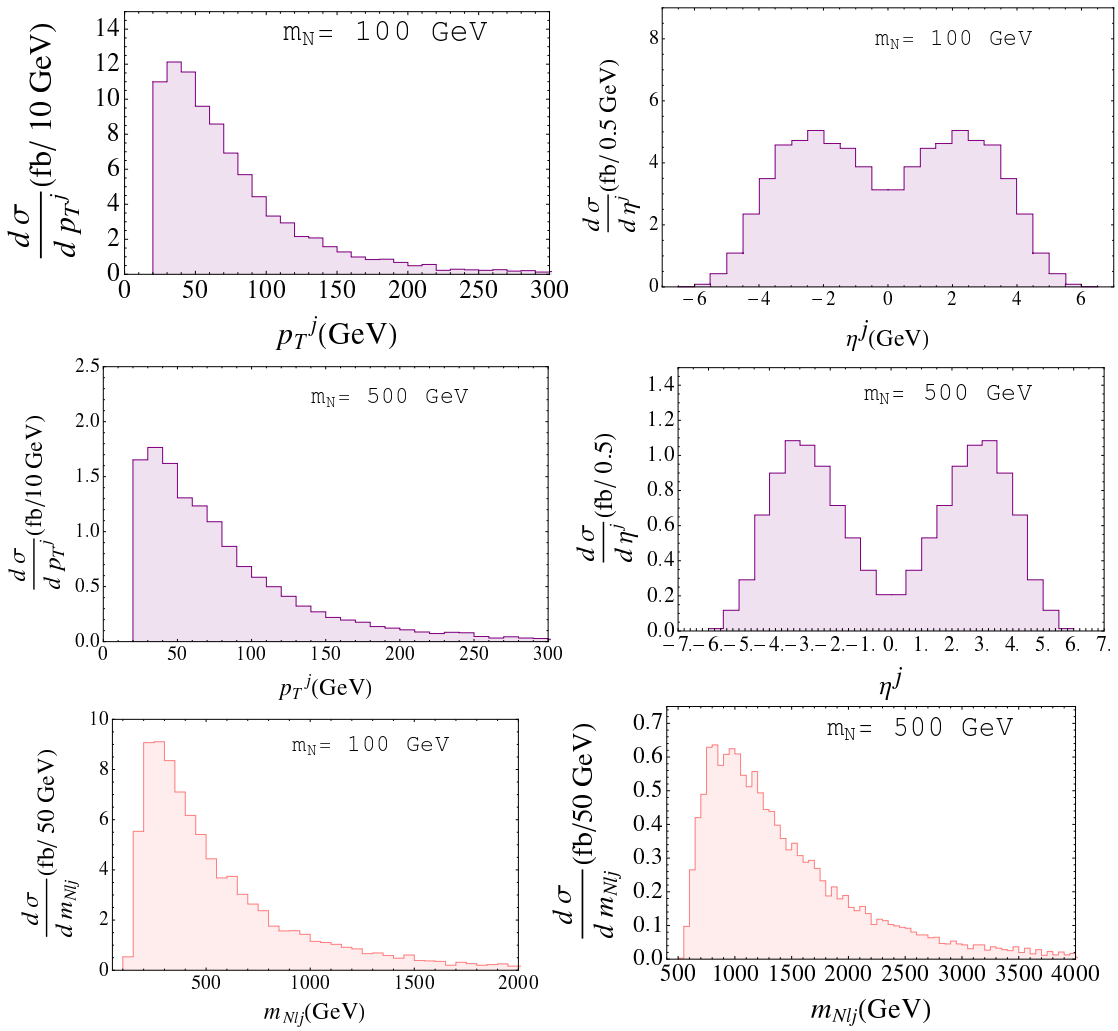

Figure 21: The first and second rows show the p_T and η distributions of the jet produced in the $N\ell j$ final state from the photon mediated elastic processes. The third row shows the final state invariant mass ($m_{N\ell j}$) distributions. The left column stands for $m_N = 100$ GeV whereas the right one is for $m_N = 500$ GeV.

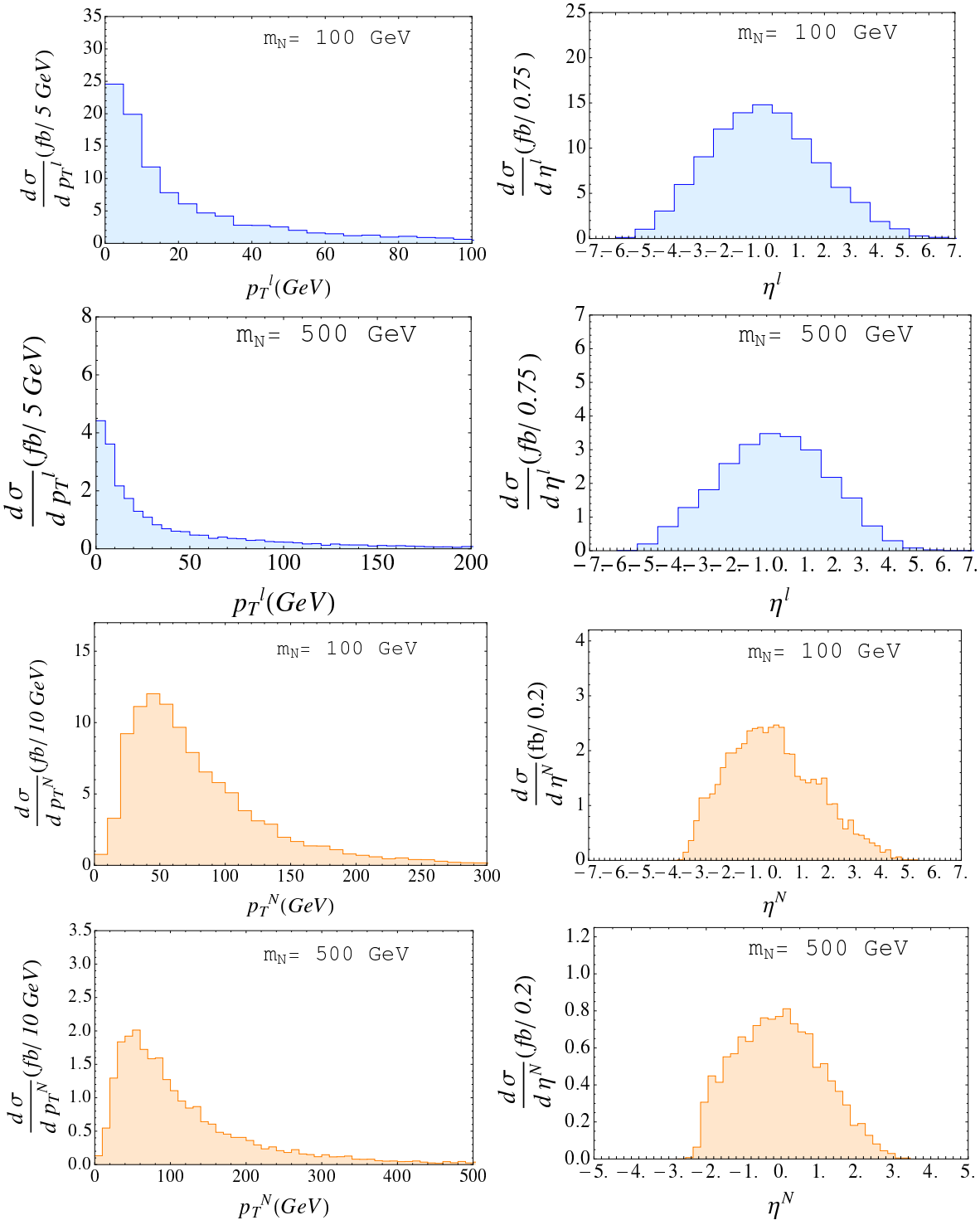

Figure 22: The first and second rows show the p_T and η distributions of the lepton produced in the $N\ell j$ final state from the photon mediated inelastic processes. The third and fourth rows show the same for the heavy neutrino. The left column stands for $m_N = 100$ GeV whereas the right one is for $m_N = 500$ GeV.

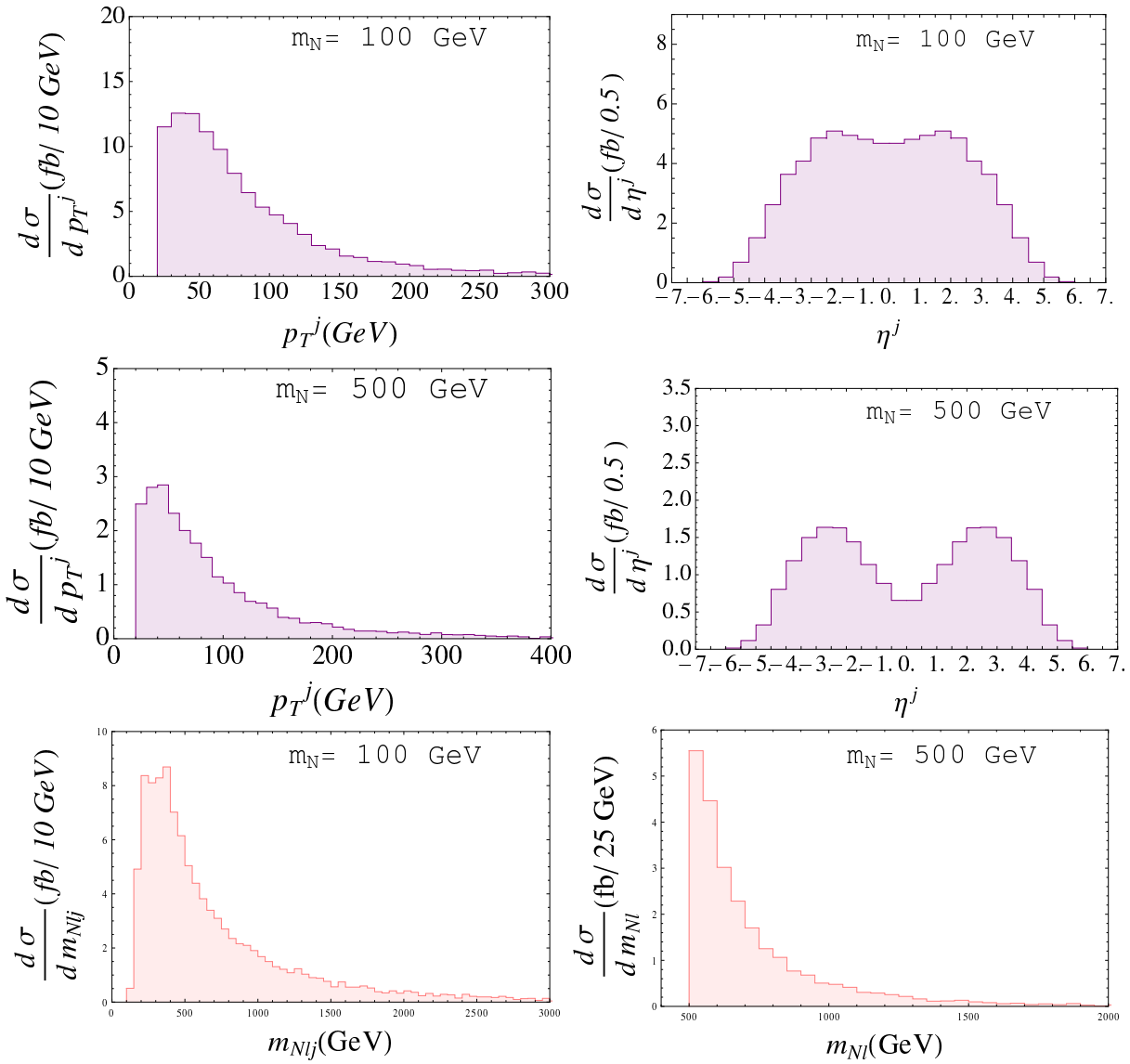

Figure 23: The first and second rows show the p_T and η distributions of the jet produced in the $N\ell j$ final state from the photon mediated inelastic processes. The third row shows the final state invariant mass ($m_{N\ell j}$) distributions. The left column stands for $m_N = 100$ GeV whereas the right one is for $m_N = 500$ GeV.

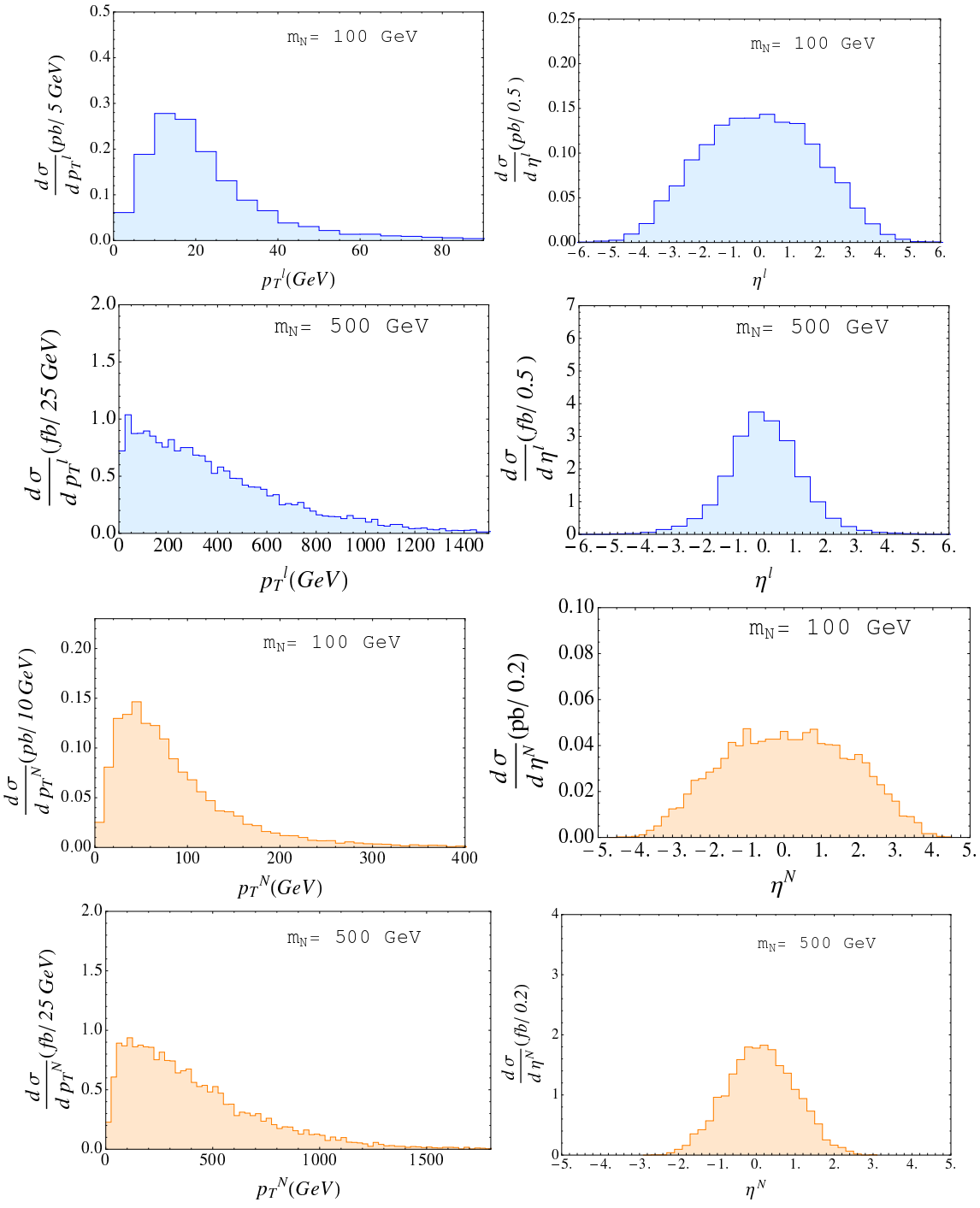

Figure 24: The first and second rows show the p_T and η distributions of the lepton produced in the $N\ell jj$ final state from the photon mediated deep-inelastic processes. The third and fourth rows show the same for the heavy neutrino. The left column is for $m_N = 100$ GeV whereas the right one stands for $m_N = 500$ GeV.

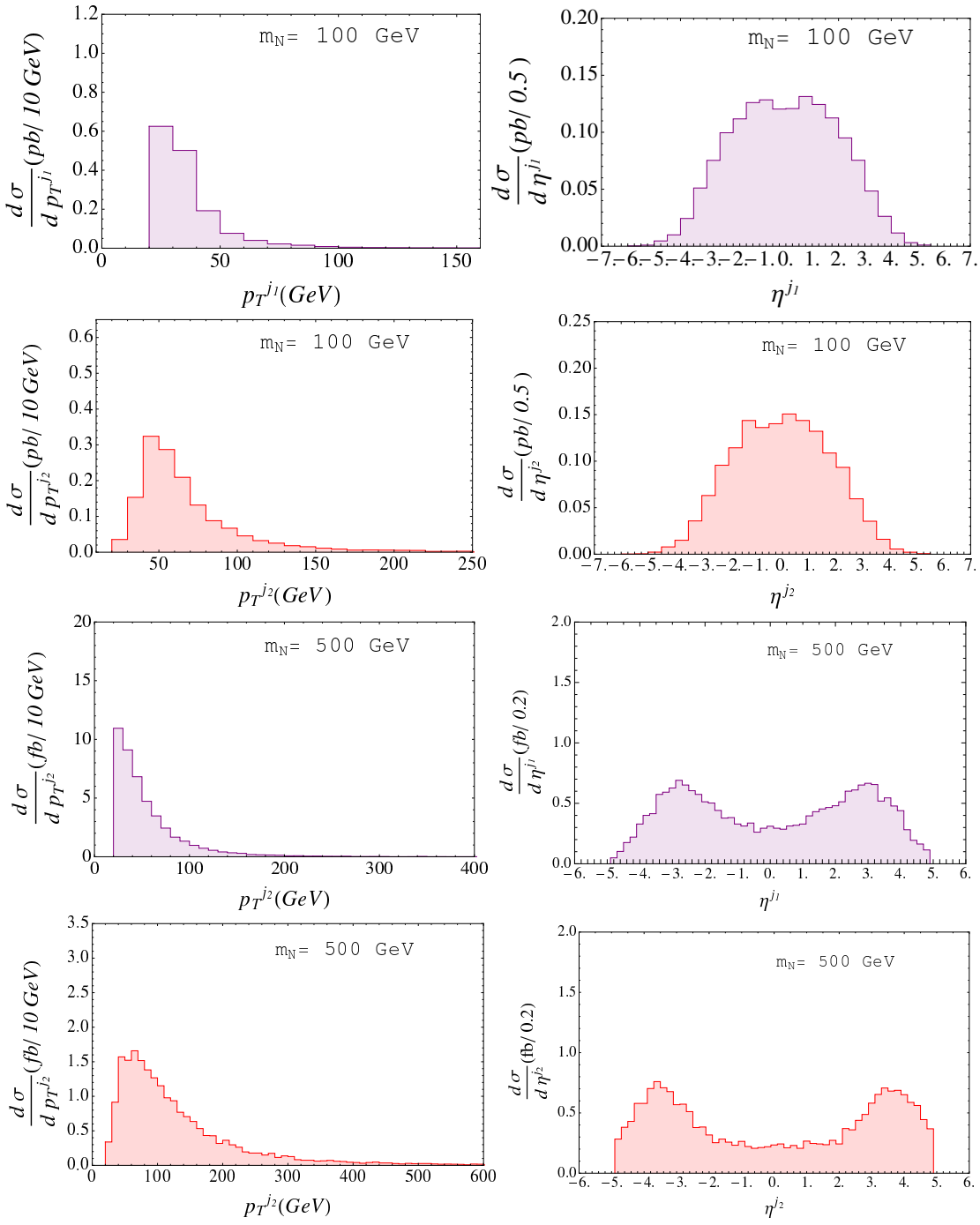

Figure 25: The first and second rows show the p_T and η distributions of the non-leading jet produced in the $N\ell jj$ final state from photon mediated deep-inelastic processes. The third and fourth rows show the same for the leading jet. The left column is for $m_N = 100$ GeV whereas the right one stands for $m_N = 500$ GeV.

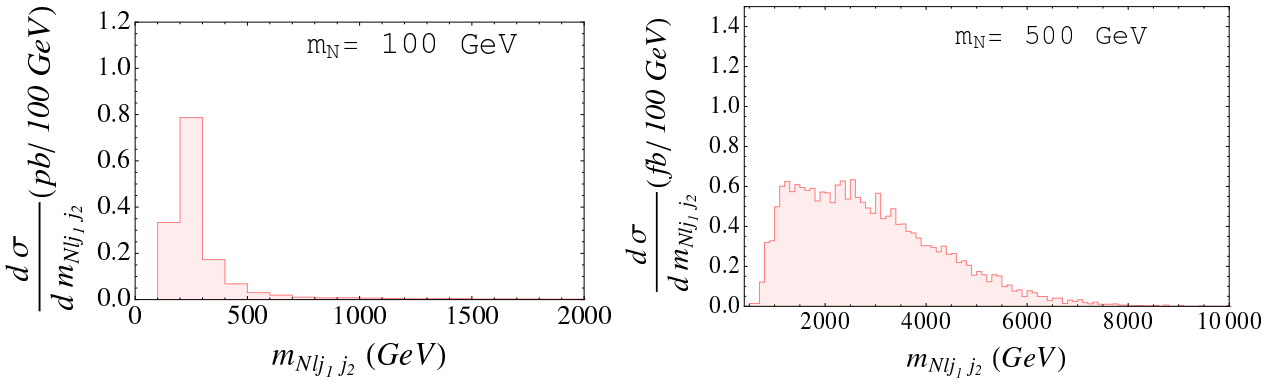

Figure 26: Figure shows the final state invariant mass ($m_{N\ell j_1 j_2}$) distributions produced in the $N\ell jj$ final state from the photon mediated deep-inelastic processes. The left panel shows $m_N = 100$ GeV whereas the right one is $m_N = 500$ GeV.

and

$$|V_{\ell N}|^2_{2-j} \lesssim \frac{\sigma^{ATLAS}}{\sigma_{0-j} + \sigma_{1-j} + \sigma_{2-j}}. \tag{9}$$

Our resultant upper bounds on the mixing angles are shown in Fig. 27, along with the bounds from ATLAS [18], CMS [19], LEP (L3) [22], electroweak precision data for electron (EWPD-e) and muon (EWPD-μ) [23]-[25], and finally LHC Higgs data (Higgs) [21]. The bound obtained from σ_{0-j} is consistent with the bound presented in [18]. We can see that a significant improvement on the bounds by adding the σ_{1-j} and σ_{2-j} cross sections. We have also calculated the cross sections, σ_{0-j}, σ_{1-j} and σ_{2-j}, for the 14 TeV LHC. Applying the ATLAS bound at 8 TeV with 20.3 fb^{-1} luminosity, we put a prospective upper bound on the mixing angles. We scaled the bound for the luminosities of 300 fb^{-1} and 1000 fb^{-1}. The results are shown in Fig 28.

Recently the CMS has performed the same-sign di-lepton plus di-jet search [19]. Using this reslt and adopting the same procedure for the ATLAS result we calculate the upper bound on the mixing angles at the 8 TeV LHC. The results are shown in Fig. 29. A significant improvement for the upper bound on the mixing angle is obtained by adding the σ_{1-j} and σ_{2-j} results to the σ_{0-j} case. We can see that at the low mass region the bound obtained by the CMS analysis is comparable to our 0-jet plus 1-jet case and in the high mass region that is comparable to our 0-jet case. Using the 8 TeV CMS result [19] we obtain prospective bound at the 14 TeV for the luminosities of 20.3 fb^{-1}, 300 fb^{-1} and 1000 fb^{-1}. The results are shown in Fig. 30.

5.2. Tri-lepton signal

In this analysis we consider two cases. One is the Flavor Diagonal case (FD), where we introduce three generations of the degenerate heavy neutrinos and each generation couples

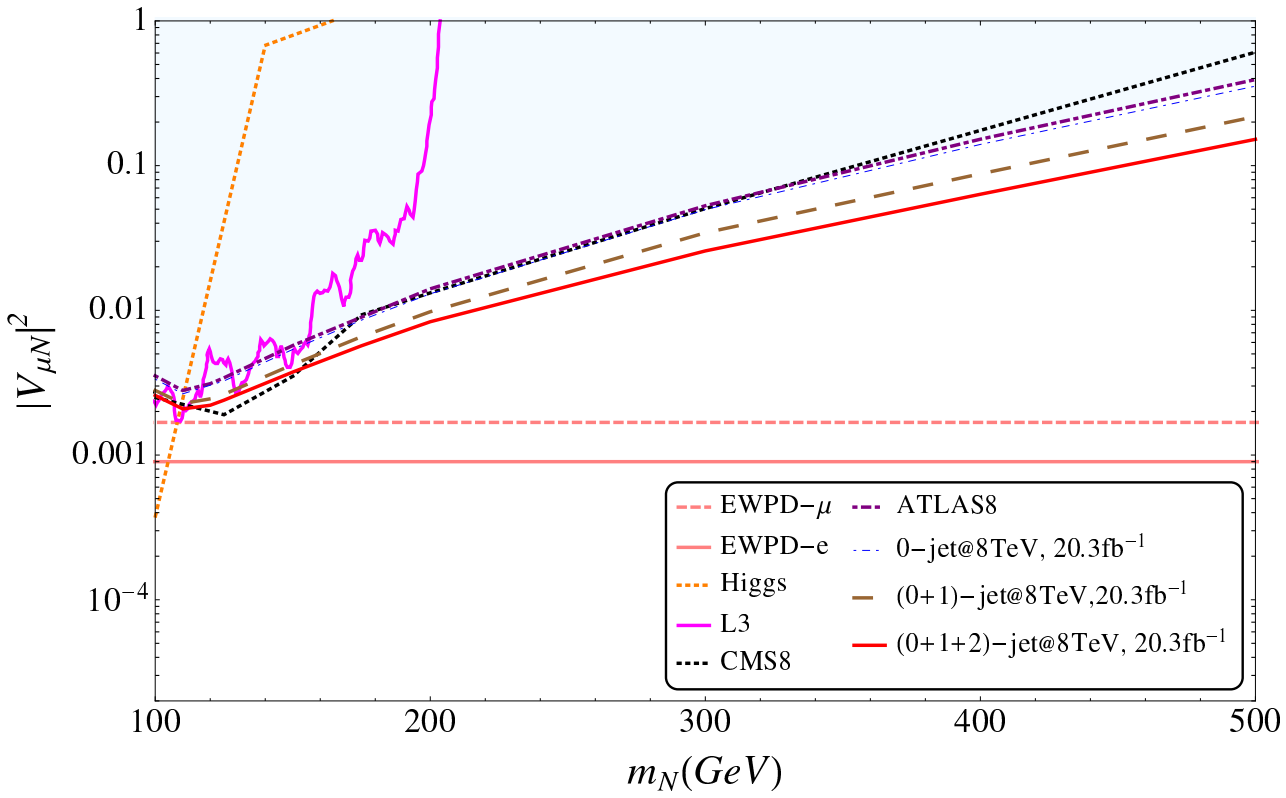

Figure 27: Figure shows the upper bounds of square on the mixing angles as a function of m_N using the ATLAS data at the 8 TeV [18]. The 0-jet (0-jet8, 20.3 fb^{-1}) result is compared with the ATLAS bounds (ATLAS8). The improved results with 1-jet ((dashed), (0+1)-jet@8TeV, 20.3 fb^{-1}) and 2-jet (thick, solid,(0+1+2)-jet@8, 20.3 fb^{-1}) are shown with respect to the bounds obtained by ATLAS [18]. These bounds are compared to (i) the χ^2-fit to the LHC Higgs data [21] (Higgs), (ii) from a direct search at LEP [22](L3), valid only for the electron flavor, (iv) CMS limits from $\sqrt{s}$ =8 TeV LHC data [19] (CMS8), for a heavy Majorana neutrino of the muon flavor and (v) indirect limit from a global fit to the electroweak precision data [23, 24, 25] (EWPD), for both electron (solid, EWPD- e) and muon (dotted, EWPD- μ) flavors. The shaded region is excluded.

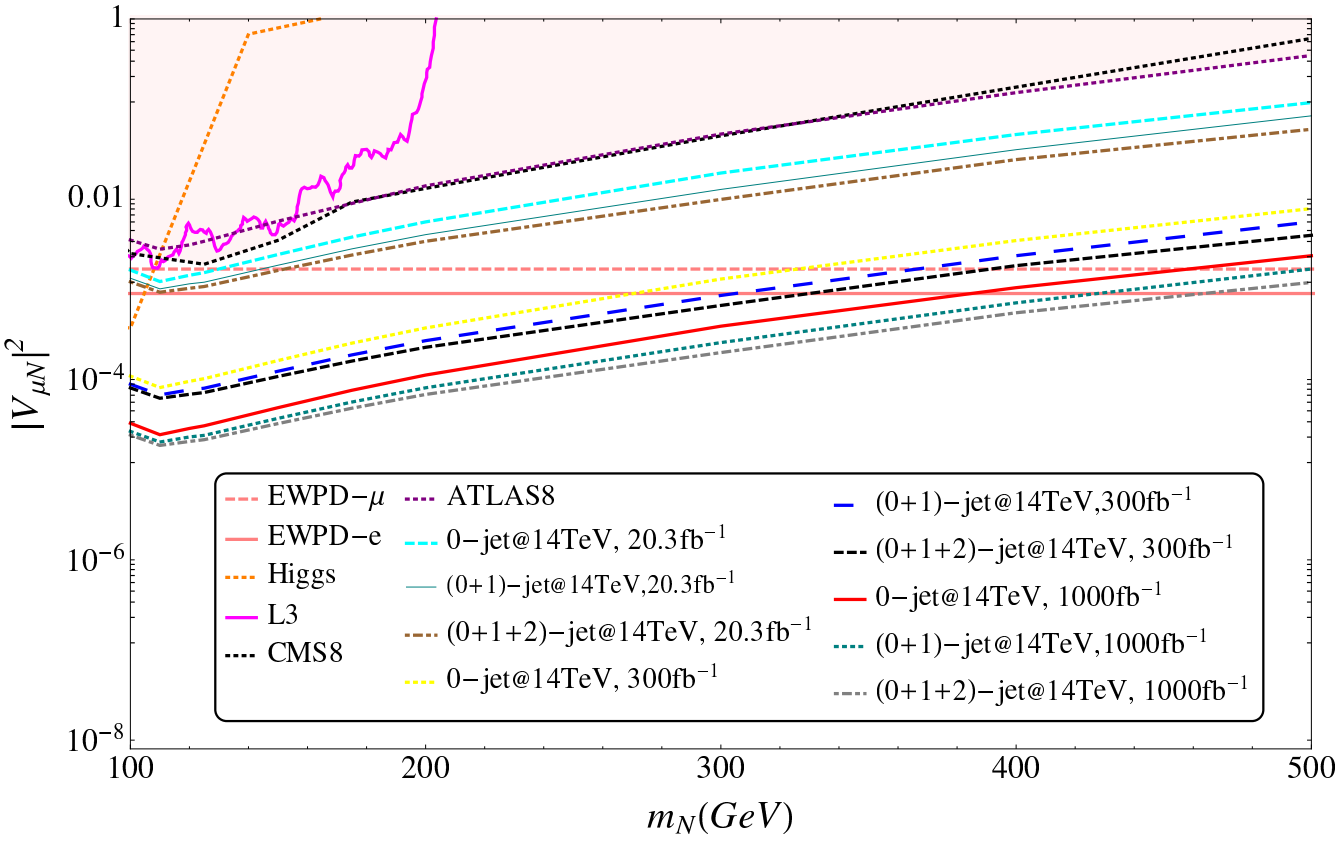

Figure 28: Figure shows the search reach for the square of the mixing angles as a function of m_N at 14 TeV LHC using the ATLAS data at the 8 TeV [18]. In this plot we give a prospective search reach for the 14 TeV. The results with 0-jet (0-jet@14TeV, 20.3 fb^{-1}), 1-jet ((0+1)-jet@14TeV, 20.3 fb^{-1}) and 2-jet ((0+1+2)-jet@14, 20.3 fb^{-1}) are shown at 20.3 fb $^{-1}$. The prospective results with 0-jet(0-jet@14TeV, 300 fb^{-1}), 1-jet ((0+ 1)-jet@14TeV, 300 fb^{-1}) and 2-jet ((0+1+2)-jet@14TeV, 300 fb^{-1}) are also plotted at 300 fb^{-1} luminosity. The prospective results with 0-jet (0-jet@14teV, 1000 fb^{-1}), 1-jet ((0+ 1)-jet@14TeV, 1000fb^{-1}) and 2-jet ((0+1+2)-jet@14TeV, 1000 fb^{-1}) are plotted at 1000 fb^{-1} and compared to (i) the χ^2-fit to the LHC Higgs data [21] (Higgs), (ii) from a direct search at LEP [22](L3), valid only for the electron flavor, (iv) CMS limits from $\sqrt{s}$ =8 TeV LHC data [19] (CMS8), for a heavy Majorana neutrino of the muon flavor and (v) indirect limit from a global fit to the electroweak precision data [23, 24, 25] (EWPD), for both electron (solid, EWPD-e) and muon (dotted, EWPD- μ) flavors. The shaded region is excluded.

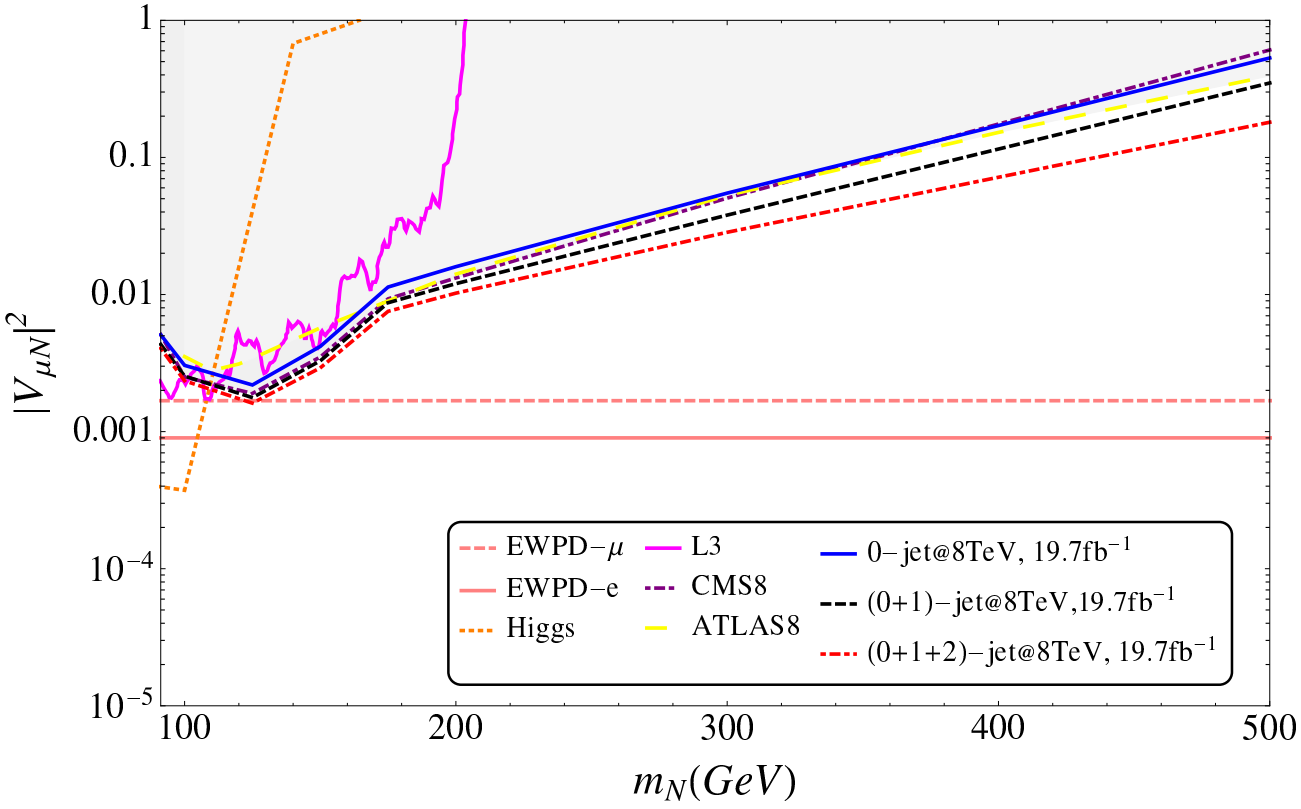

Figure 29: Figure shows the upper bounds on square of the mixing angles as a function of m_N using the CMS data at the 8 TeV [19]. The 0-jet (0-jet@8TeV, 19.7 fb^{-1}) result is compared with the CMS bounds (CMS8). The improved results with 1-jet ((0+ 1)- jet@8TeV, 19.7 fb^{-1}) and 2-jet ((0+ 1+ 2)-jet@8TeV, 19.7 fb^{-1}) are shown with respect to the CMS data from [19]. The bounds are compared to (i) the χ^2-fit to the LHC Higgs data [21] (Higgs), (ii) from a direct search at LEP [22](L3), valid only for the electron flavor, (iv) ATLAS limits from $\sqrt{s}$ =8 TeV LHC data [18] (ATLAS 8), for a heavy Majorana neutrino of the muon flavor and (v) indirect limit from a global fit to the electroweak precision data [23, 24, 25] (EWPD), for both electron (solid, EWPD-e) and muon (dotted, EWPD- μ) flavors. The shaded region is excluded.

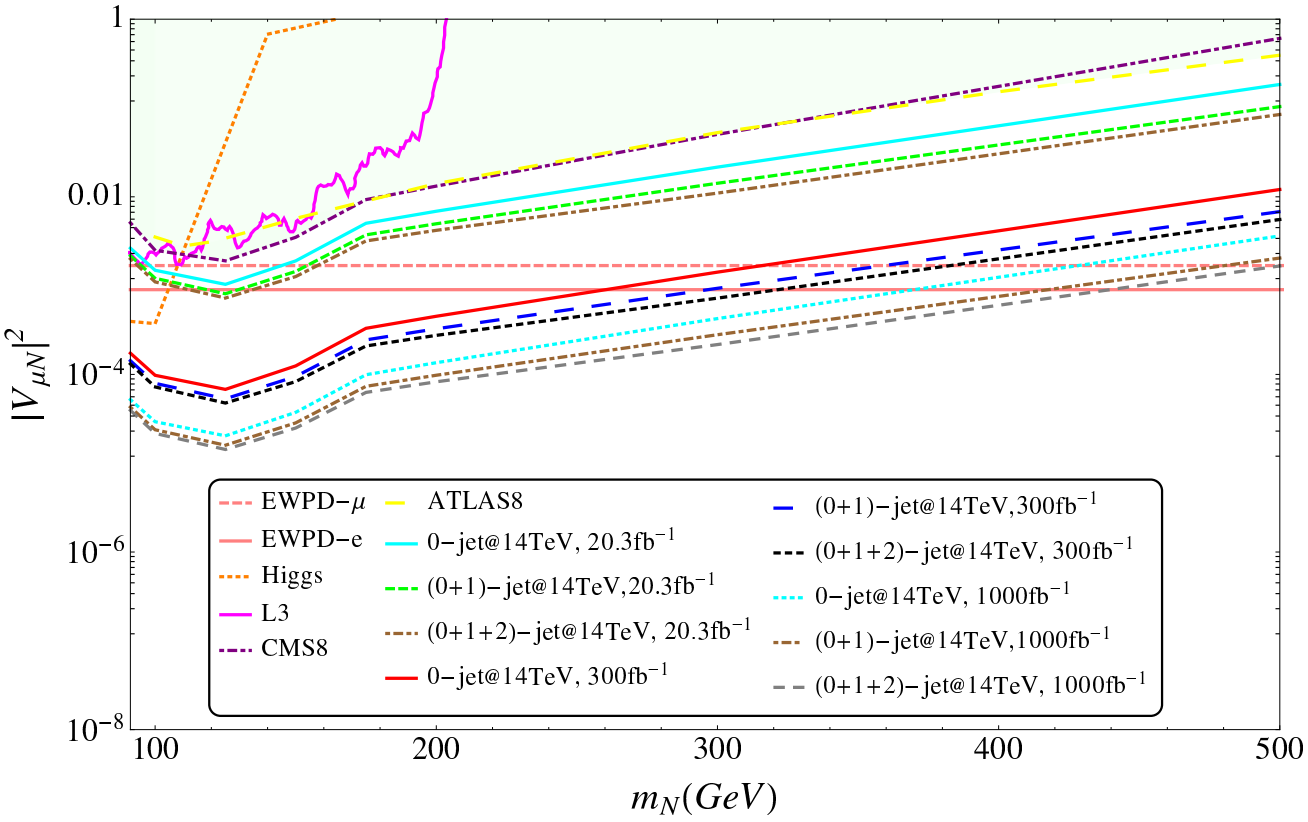

Figure 30: Figure shows the prospective search reach for square of the mixing angles as a function of m_N at the 14 TeV LHC using the CMS data at the 8 TeV [19]. The 0-jet (0-jet@14TeV, 20.3 fb^{-1}), 1-jet ((0+1)-jet@14TeV, 20.3 fb^{-1})and 2-jet ((0+1+2)-jet@14TeV, 20.3 fb^{-1}) are shown at the 20.3 fb^{-1}. The prospective results with 0-jet(0-jet@14TeV, 300 fb^{-1}), 1-jet ((0+ 1)-jet@14TeV, 300 fb^{-1}) and 2-jet ((0+1+2)-jet@14TeV, 300 fb^{-1}) are also plotted at 300 fb^{-1} luminosity. The prospective results with 0-jet (0-jet@14TeV, 1000 fb^{-1}), 1-jet ((0+ 1)-jet@14TeV, 1000fb^{-1}) and 2-jet ((0+1+2)-jet@14TeV, 1000 fb^{-1}) are plotted at 1000 fb^{-1} and compared to (i) the χ^2-fit to the LHC Higgs data [21] (Higgs), (ii) from a direct search at LEP [22](L3), valid only for the electron flavor, (iv) CMS limits from $\sqrt{s}$ =8 TeV LHC data [19] (CMS8), for a heavy Majorana neutrino of the muon flavor and (v) indirect limit from a global fit to the electroweak precision data [23, 24, 25] (EWPD), for both electron (solid, EWPD- e) and muon (dotted, EWPD- μ) flavors. The shaded region is excluded.

with the single, corresponding lepton flavor. The other one is the Single Flavor case (SF) where only one heavy neutrino is light and accessible to the LHC which couples to only the first or second generation of the lepton flavor. In this analysis we use the `CTEQ6L PDF` [90]. We have calculated the bound on the mixing angle for the tri-lepton case using the $N\ell j$ final state in [28]. In the following we extend this analysis by adding the photon mediated processes to the $N\ell j$ final state. We also include the $N\ell jj$ final state.

We generate the 1-jet and the 2-jet parton level processes separately in `MadGraph` and then gradually hadronize and perform detector simulations with `Xqcut`= $p_T^j = 30$ GeV and `QCUT`= 36 GeV for the hadronization. In our analysis we use the matched cross section after the detector level analysis. After the signal events are generated we adopt the following basic criteria, used in the CMS tri-lepton analysis [20]:

(i) The transverse momentum of each lepton: $p_T^\ell > 10$ GeV.

(ii) The transverse momentum of at least one lepton: $p_T^{\ell,\text{leading}} > 20$ GeV.

(iii) The jet transverse momentum: $p_T^j > 30$ GeV.

(iv) The pseudo-rapidity of leptons: $|\eta^\ell| < 2.4$ and of jets: $|\eta^j| < 2.5$.

(v) The lepton-lepton separation: $\Delta R_{\ell\ell} > 0.1$ and the lepton-jet separation: $\Delta R_{\ell j} > 0.3$.

(vi) The invariant mass of each OSSF (opposite-sign same flavor) lepton pair: $m_{\ell^+\ell^-} < 75$ GeV or > 105 GeV to avoid the on-Z region which was excluded from the CMS search. Events with $m_{\ell^+\ell^-} < 12$ GeV are rejected to eliminate background from low-mass Drell-Yan processes and hadronic decays.

(vii) The scalar sum of the jet transverse momenta: $H_T < 200$ GeV.

(viii) The missing transverse energy: $\not{E}_T < 50$ GeV.

The additional tri-lepton contributions come from $N \to Z\nu, h\nu$, followed by the Z, h decays into a pair of OSSF leptons. However, the Z contribution is rejected after the implementation of the invariant mass cut for the OSSF leptons to suppress the SM background and the h contribution is suppressed due to very small Yukawa couplings of electrons and muons. Using different values of $\not{E}_T$ and H_T, the CMS analysis provides different number of observed events and the corresponding SM background expectations. For our analysis the set of cuts listed above are the most efficient ones as implemented by the CMS analysis [20]. To derive the limits on $|V_{\ell N}|^2$, we calculate the signal cross section normalized by the square of the mixing angle as a function of the heavy neutrino mass m_N for both SF and FD cases, by imposing the CMS

selection criteria listed above. The corresponding number of signal events passing all the cuts is then compared with the observed number of events at the 19.5 fb^{-1} luminosity [20]. For the selection criteria listed above, the CMS experiment observed:

(a) 510 events with the SM background expectation of 560±87 events for $m_{\ell^+\ell^-} < 75$ GeV.

(b) 178 events with the SM background expectation of 200±35 events for $m_{\ell^+\ell^-} > 105$ GeV.

In case (a) we have an upper limit of 37 signal events, while in case (b) leads to an upper limit of 13 signal events. Using these limits, we can set an upper bound on $|V_{\ell N}|^2$ for a given value of m_N.

In Fig. 31 we plot our results of the upper bound for the SF and FD cases. The thick red dashed line ($SF8_f^{75}$) stands for the results of the SF case by employing the CMS observation (a) whereas the thick red solid line ($SF8_f^{105}$) stands for the results of the SF case by employing the CMS observation (b). The corresponding results for the FD case are represented by the thick blue dashed line ($FD8_f^{75}$) and the thick blue solid line ($FD8_f^{105}$), respectively. The results of the previous analysis [28] are shown by the yellow dashed lines ($SF8_i^{75}$, $SF8_i^{105}$, $FD8_i^{75}$ and $FD8_i^{105}$). Our new results have improved the upper bound on the mixing angles. This improvement becomes more significant in the high m_N region because the photon mediated process dominates the N production cross section (compare Figs. 4, 9 and 13 each other). We have also calculated the cross sections at the 14 TeV LHC. Comparing the cross sections at 14 TeV to those at 8 TeV we have obtained the prospective upper bounds at the 14 TeV LHC, which are shown as the thin solid lines ($SF14_f^{105}$ and $FD14_f^{105}$) above the Z-pole.

6. Conclusion

We have studied the productions of heavy Majorana and pseudo-Dirac neutrinos from the type-I and the inverse seesaw mechanisms, respectively. The heavy neutrinos can be produced at the LHC through the sizable mixings with the light neutrinos in the SM. For the heavy neutrino production process, we have considered various initial states such as $q\overline{q'}$, qg and gg as well as photon mediated processes to produce the final states $N\ell$, $N\ell j$ and $N\ell jj$. We have found that the cross section to produce $N\ell j$ from the $q\overline{q'}$ initial state dominates over the qg for $m_N \gtrsim 150$ GeV, while the qg initial state takes over for $m_N \lesssim 150$ GeV at the 8 TeV LHC. This happens because at low Bjorken scaling parameter the gluon PDF dominates over the quark PDF. For the final state $N\ell jj$ the cross section obtained from qg dominates over that from the $q\overline{q'}$ for $m_N \lesssim 200$ GeV, while for $m_N \gtrsim 200$ GeV the $q\overline{q'}$ dominates. The gluon fusion channel follows the cross sections from the qg and $q\overline{q'}$ initial states. The gluon fusion channel can not dominate for the m_N values we studied, because in order to produce the heavy neutrino the

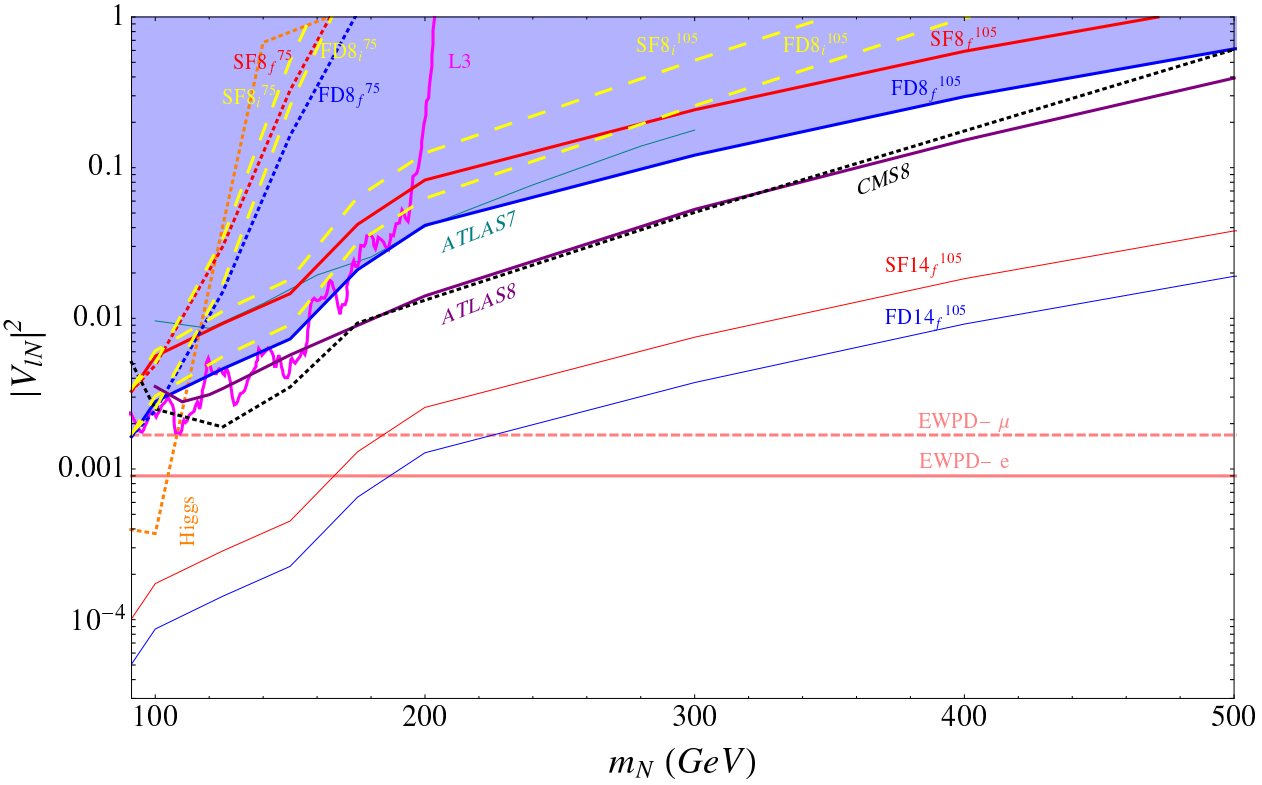

Figure 31: The 95 % CL upper limits on the light-heavy neutrino mixing angles $|V_{\ell N}|^2$ as a function of the heavy Dirac neutrino mass m_N, derived from the CMS tri-lepton data at $\sqrt{s}$ =8 TeV LHC for 19.5 fb^{-1} luminosity [20]. The exclusion (shaded) regions are shown for two benchmark scenarios: (i) single flavor (SF) and (ii) flavor diagonal (FD), with two choices of the selection cut $m_{l^+l^-}$<75 GeV (thick dotted) and >105 GeV (thick solid). The previous results with the selection cut $m_{l^+l^-}$<75 GeV (thick dot-dashed) and >105 GeV (thick large-dashing) at the 1-jet level are shown in this context from [28]. The corresponding conservative projected limits from $\sqrt{s}$ =14 TeV LHC data with 300 fb^{-1} integrated luminosity are shown by thin solid lines ($SF14_f^{105}$ and $FD14_f^{105}$) above the Z-pole. Some relevant existing upper limits (all at 95% CL) are also shown for comparison: (i) from a χ^2-fit to the LHC Higgs data [21] (Higgs), (ii) from a direct search at LEP [22](L3), valid only for the electron flavor, (iii) ATLAS limits from $\sqrt{s}$ =7 TeV LHC data [17] (ATLAS7) and $\sqrt{s}$ =8 TeV LHC data [18] (ATLAS8), valid for a heavy Majorana neutrino of the muon flavor, (iv) CMS limits from $\sqrt{s}$ =8 TeV LHC data [19] (CMS8), for a heavy Majorana neutrino of the muon flavor and (v) indirect limit from a global fit to the electroweak precision data [23, 24, 25] (EWPD), for both electron (solid) and muon (dotted) flavors. The data for 1-jet case from [28] are shown by SF_i^{75}, SF_i^{105}, $FD_i^{75}$and FD_i^{105} (large dashed lines). The shaded region is excluded.

Bjorken scaling parameters for the two gluons can not be small simultaneously. We have also studied the photon mediated processes such as elastic, inelastic and the deep-inelastic processes. For $m_N \lesssim 400$ (300) GeV, the deep-inelastic process dominates over the other photon mediated processes for $p_T^j \gtrsim 10$ (20) GeV. The inelastic process dominates over the deep-inelastic process for $m_N \gtrsim 400$ (300) for $p_T^j \gtrsim 10$ (20) GeV. The elastic process always yields the lowest cross section.

We have showed the kinematic distributions of the heavy neutrino produced with the associated leptons and jets for $m_N = 100$ GeV and $m_N = 500$ GeV. We have plotted the differential scattering cross sections as a function of p_T and η of the heavy neutrino, associated lepton and the jets, and the invariant mass distributions for the final states. The p_T^ℓ distribution has a peak around $\frac{m_N}{5}$ for the $q\overline{q'}$, qg and gg initial states, while for the photon mediated processes the distribution is found to be almost independent of m_N. The η^ℓ distributions of the leptons are peaked around 0 for all the initial states and become sharper with the increase in m_N. The p_T and η distributions of the heavy neutrinos are similar to those of the leptons irrespective of the initial states. The p_T distributions of the jets start from cut values used in the analysis for final states with single and two-jets. The p_T^j distributions for the $N\ell j$ final state from the $q\overline{q'}$ and qg initial states sharply drop with respect to those for the $N\ell jj$ final state from the $q\overline{q'}$, qg and gg initial states. In case of the photon mediated processes the p_T distributions of the jets are observed to have peaks around $\frac{m_W}{2}$ for the $N\ell j$ final state from the elastic, inelastic cases and the leading jet from the $N\ell jj$ final state from the deep-inelastic process. The η distributions of the leading and non-leading jets of the photon mediated processes show the distinct double peaks at the forward backward regions. This is a typical feature of the photon mediated process. We notice that the invariant mass distributions of the different final states sharply peak at the vicinity of the heavy neutrino mass, referring to the production of the heavy neutrino almost at rest.

We have studied the collider signatures of Majorana and pseudo-Dirac heavy neutrinos. From the Majorana heavy neutrino we consider the same-sign di-lepton plus di-jet in the final state. We have generated the signal cross sections by using `MadGraph`. We compare our results with the recent ATLAS [18] and CMS [19] data at $\sqrt{s} = 8$ TeV with 20.3 fb^{-1} and 19.7 fb^{-1} luminosities, respectively, we have obtained the upper bound on the mixing angles. Using a variety of the initial states we have improved the upper bounds previously obtained in [18] and [19]. For the pseudo-Dirac heavy neutrino we have generated the tri-lepton plus missing energy as the signal events using `MadGraph` and performed the detector simulation for various initial states. Comparing our simulation results with the recent anomalous multi-lepton search results by CMS [20] at $\sqrt{s} = 8$ TeV with 19.5 fb^{-1} luminosity we have obtained the upper bound on

the mixing angles, which improves the previously given result in [28]. Finally we have scaled our results at the 8 TeV LHC to obtain a prospective search reach at the 14 TeV LHC with higher luminosities.

Acknowledgements

The authors cordially thank P. S. Bhupal Dev for his collaboration in the earlier stage of the project. AD would like to thank Valentin Hirschi for useful discussions on `MadGraph`. This work is supported in part by the United States Department of Energy Grant, No. DE-SC 0013680.

References

[1] J. Beringer et. al. [Particle Data Group Collaboration], Phys. Rev. D 86, 010001 (2012).
[2] K. Abe et. al. [T2K Collaboration] Phys. Rev. Lett. 107, 041801 (2011).
[3] P. Adamson et al. [MINOS Collaboration], Phys. Rev. Lett. 107, 181802 (2011).
[4] Y. Abe et al. [DOUBLE-CHOOZ Collaboration], Phys. Rev. Lett. 108, 131801 (2012).
[5] F. P. An et al. [DAYA-BAY Collaboration], Phys. Rev. Lett. 108, 171803 (2012).
[6] J. K. Ahn et al. [RENO Collaboration], Phys. Rev. Lett. 108, 191802 (2012).
[7] P. Minkowski, "$\mu \to e\gamma$ at a Rate of One Out of 10^9 Muon Decays?," Phys. Lett. B **67**, 421 (1977).
[8] T. Yanagida, in Proceedings of the Work- shop on the Unified Theory and the Baryon Number in the Universe (O. Sawada and A. Sugamoto, eds.), KEK, Tsukuba, Japan, 1979, p. 95;
[9] M. Gell-Mann, P. Ramond, and R. Slansky, Supergravity (P. van Nieuwenhuizen et al. eds.), North Holland, Amsterdam, 1979, p. 315;
[10] S. L. Glashow, The future of elementary particle physics, in Proceedings of the 1979 Carg'ese Summer Institute on Quarks and Leptons (M. Levy et al. eds.), Plenum Press, New York, 1980, p. 687;
[11] R. N. Mohapatra and G. Senjanovic, "Neutrino Mass and Spontaneous Parity Violation," Phys. Rev. Lett. **44**, 912 (1980).
[12] T. Saito *et al.*, "Extra dimensions and Seesaw Neutrinos at the International Linear Collider," Phys. Rev. D **82**, 093004 (2010) [arXiv:1008.2257 [hep-ph]]
[13] S. Banerjee, P. S. B. Dev, A. Ibarra, T. Mandal and M. Mitra,"Prospects of Heavy Neutrino Searches at Future Lepton Colliders," arXiv:1503.05491 [hep-ph].
[14] J. A. Casas and A. Ibarra, "Oscillating neutrinos and muon $--->$ e, gamma," Nucl. Phys. B **618**, 171 (2001)[hep-ph/0103065].
[15] R. N. Mohapatra, Phys. Rev. Lett. 56 (1986) 561.
[16] R. N. Mohapatra and J. W. F. Valle, Phys. Rev. D 34, 1642 (1986).
[17] ATLAS Collaboration, ATLAS-CONF-2012-139. S. Chatrchyan, CMS Collaboration, et al. For a similar analysis (with weaker limits), see Phys. Lett. B, 717 (2012), p. 109, arXiv:1207.6079 [hep-ph].
[18] G. Aad *et al.* [ATLAS Collaboration], "Search for heavy Majorana neutrinos with the ATLAS detector in pp collisions at $\sqrt{s} = 8$ TeV," arXiv:1506.06020 [hep-ex].
[19] V. Khachatryan *et al.* [CMS Collaboration], "Search for heavy Majorana neutrinos in $\mu^{\pm}\mu^{\pm}$+jets events in proton-proton collisions at $\sqrt{s} = 8$ TeV,"arXiv:1501.05566 [hep-ex].
[20] CMS Collaboration, arXiv:1404.5801 [hep-ex]; For an earlier analysis with $\sqrt{s} = 7$ TeV LHC data, see S. Chatrchyan, *et al.*, CMS Collaboration, J. High Energy Phys. 1206 (2012) 169, arXiv: 1204.5341 [hep-ex].
[21] P. S. B. Dev, R. Franceschini, R. N. Mohapatra, Phys. Rev. D, 86 (2012), p. 093010, arXiv:1207.2756 [hep-ph].
[22] P. Achard, L3 Collaboration, et al., Phys. Lett. B, 517 (2001), p. 67, arXiv:hep-ex/0107014.
[23] J. de Blas, Europhys. J. Web Conf., 60 (2013), p. 19008, arXiv:1307.6173 [hep-ph],
[24] F. del Aguila, J. de Blas, M. Perez-Victoria. For earlier fits, see Phys. Rev. D, 78 (2008), p. 013010, arXiv:0803.4008 [hep-ph].

[25] E. Akhmedov, A. Kartavtsev, M. Lindner, L. Michaels, J. Smirnov, J. High Energy Phys., 1305 (2013), p. 081, arXiv:1302.1872 [hep-ph]
[26] L. Basso, O. Fischer and J. J. van der Bij, "Precision tests of unitarity in leptonic mixing," Europhys. Lett. **105**, no. 1, 11001 (2014), [arXiv:1310.2057 [hep-ph]].
[27] S. Antusch and O. Fischer, "Non-unitarity of the leptonic mixing matrix: Present bounds and future sensitivities,"JHEP **1410**, 94 (2014), [arXiv:1407.6607 [hep-ph]].
[28] A. Das, P. S. Bhupal Dev, N. Okada," Direct bounds on electroweak scale pseudo- Dirac neutrinos from $\sqrt{s}$ =8 TeV LHC data", Phys. Lett. B **735** (2014) 364-370
[29] T. Yanagida, "Horizontal Symmetry and Masses of Neutrinos," Prog. Theor. Phys. **64**, 1103 (1980).
[30] J. Schechter and J. W. F. Valle, "Neutrino Masses in SU(2) x U(1) Theories," Phys. Rev. D **22**, 2227 (1980).
[31] A. Das, N. Okada,"Inverse seesaw neutrino signatures at the LHC and ILC", Phys. Rev. D **88**, 113001, (2013)
[32] J. Alwall, M. Herquet, F. Maltoni, O. Mattelaer and T. Stelzer, "MadGraph 5 : Going Beyond," JHEP **1106**, 128 (2011)[arXiv:1106.0522 [hep-ph]].
[33] J. Alwall, M. Herquet, F. Maltoni, O. Mattelaer, T. Stelzer, J. High Energy Phys. 1106 (2011) 128, arXiv: 1106.0522 [hep-ph]
[34] J. Alwall, R. Frederix, S. Frixione, V. Hirschi, F. Maltoni, O. Mattelaer, H.-S. Shao and T. Stelzer *et al.*, "The automated computation of tree-level and next-to-soft order differential cross sections, and their matching to parton shower simulations," J. High Energy Phys. **1407**, 079 (2014) [arXiv:1405.0301 [hep-ph]].
[35] A. Pilaftsis and T. E. J. Underwood, Nucl. Phys. B 692, 303 (2004) [hep-ph/0309342];
[36] J. Kersten and A. Y. Smirnov, Phys. Rev. D 76, 073005 (2007) [arXiv:0705.3221 [hep-ph]];
[37] Z.-z. Xing, Prog. Theor. Phys. Suppl. 180, 112 (2009) [arXiv:0905.3903 [hep-ph]];
[38] X.-G. He, S. Oh, J. Tandean and C. -C. Wen, Phys. Rev. D 80, 073012 (2009) [arXiv:0907.1607 [hep-ph]];
[39] A. Ibarra, E. Molinaro and S. T. Petcov, JHEP 1009, 108 (2010) [arXiv:1007.2378 [hep- ph]];
[40] F. F. Deppisch and A. Pilaftsis, Phys. Rev. D 83, 076007 (2011) [arXiv:1012.1834 [hep-ph]];
[41] P. S. B. Dev, C.-H. Lee and R. N. Mohapatra, Phys. Rev. D 88, 093010 (2013) [arXiv:1309.0774 [hep-ph]].
[42] A. Datta, M. Guchait and A. Pilaftsis, Phys. Rev. D 50, 3195 (1994) [hep-ph/9311257];
[43] T. Han and B. Zhang, Phys. Rev. Lett. 97, 171804 (2006) [hep-ph/0604064];
[44] S. Bray, J. S. Lee and A. Pilaftsis, Nucl. Phys. B 786, 95 (2007) [hep-ph/0702294];
[45] F. del Aguila, J. A. Aguilar-Saavedra and R. Pittau, JHEP 0710, 047 (2007) [hep-ph/0703261].
[46] F. del Aguila, J. A. Aguilar-Saavedra and R. Pittau, "Heavy neutrino signals at large hadron colliders," JHEP **0710**, 047 (2007) [hep-ph/0703261].
[47] F. del Aguila and J. A. Aguilar-Saavedra, "Distinguishing seesaw models at LHC with multi-lepton signals," Nucl. Phys. B **813**, 22 (2009) [arXiv:0808.2468 [hep-ph]].
[48] F. del Aguila and J. A. Aguilar-Saavedra, "Electroweak scale seesaw and heavy Dirac neutrino signals at LHC," Phys. Lett. B **672**, 158 (2009) [arXiv:0809.2096 [hep-ph]].
[49] G. Bambhaniya, S. Khan, P. Konar and T. Mondal, "Constraints on a seesaw model leading to quasi-degenerate neutrinos and signatures at the LHC," Phys. Rev. D **91**, no. 9, 095007 (2015) [arXiv:1411.6866 [hep-ph]].
[50] G. Bambhaniya, S. Goswami, S. Khan, P. Konar and T. Mondal, "Looking for hints of a reconstructible seesaw model at the Large Hadron Collider," Phys. Rev. D **91**, 075007 (2015) [arXiv:1410.5687 [hep-ph]].
[51] E. Arganda, M. J. Herrero, X. Marcano and C. Weiland, "Exotic $\mu\tau jj$ events from heavy ISS neutrinos at the LHC," arXiv:1508.05074 [hep-ph].
[52] M. Drewes, "The Phenomenology of Right Handed Neutrinos," Int. J. Mod. Phys. E **22**, 1330019 (2013) [arXiv:1303.6912 [hep-ph]].
[53] M. Drewes, "Theoretical Status of Neutrino Physics," arXiv:1502.06891 [hep-ph].
[54] M. Drewes and B. Garbrecht, "Experimental and cosmological constraints on heavy neutrinos," arXiv:1502.00477 [hep-ph].
[55] S. M. Boucenna, S. Morisi and J. W. F. Valle, "The low-scale approach to neutrino masses," arXiv:1404.3751 [hep-ph].
[56] F. F. Deppisch, P. S. B. Dev and A. Pilaftsis, "Neutrinos and Collider Physics," arXiv:1502.06541 [hep-ph].

[57] S. Alekhin *et al.*, "A facility to Search for Hidden Particles at the CERN SPS: the SHiP physics case," arXiv:1504.04855 [hep-ph].
[58] M. Aoki, N. Haba and R. Takahashi, "A model realizing inverse seesaw and resonant leptogenesis," arXiv:1506.06946 [hep-ph].
[59] P. Humbert, M. Lindner and J. Smirnov, "The Inverse Seesaw in Conformal Electro-Weak Symmetry Breaking and Phenomenological Consequences," JHEP **1506**, 035 (2015) [arXiv:1503.03066 [hep-ph]].
[60] M. Lindner, S. Schmidt and J. Smirnov, "Neutrino Masses and Conformal Electro-Weak Symmetry Breaking," JHEP **1410**, 177 (2014) [arXiv:1405.6204 [hep-ph]].
[61] J. N. Ng, A. de la Puente and B. W. P. Pan, "Search for Heavy Right-Handed Neutrinos at the LHC and Beyond in the Same-Sign Leptons Final State," arXiv:1505.01934 [hep-ph].
[62] D. Boyanovsky, "Nearly degenerate heavy sterile neutrinos in cascade decay: mixing and oscillations," Phys. Rev. D **90**, no. 10, 105024 (2014) [arXiv:1409.4265 [hep-ph]].
[63] B. Batell and M. McCullough, "Neutrino Masses from Neutral Top Partners," arXiv:1504.04016 [hep-ph].
[64] E. Izaguirre and B. Shuve, "Multilepton and Lepton Jet Probes of Sub-Weak-Scale Right-Handed Neutrinos," Phys. Rev. D **91**, no. 9, 093010 (2015) [arXiv:1504.02470 [hep-ph]].
[65] R. Frederix and S. Frixione, "Merging meets matching in MC@NLO," J. High Energy Phys. **1212**, 061 (2012) [arXiv: 1209.6215 [hep-ph]].
[66] S. Hoeche, F. Krauss, N. Lavesson, L. Lonnblad, M. Mangano, A. Schalicke, S. Schumann, arXiv: hep-ph/0602031;
[67] J. Alwall, *et al.*, Eur. Phys. J. C 53 (2008) 473, arXiv: 0706. 2569 [hep-ph];
[68] J. Alwall, S. de Visscher, F. Maltoni, J. High Energy Phys. 0902 (2009) 017, arXiv: 0810.5350 [hep-ph].
[69] J. Alwall *et al.* "Comperative study of various algorithms for the merging of parton showers and matrix elements in hadronic collisions," Eur. Phys. J. C **53**, 473500 (2008)
[70] P. S. B. Dev, A. Pilaftsis, U. K. Yang, Phys. Rev. Lett. 112 (2014) 081801, arXiv: 1308.2209 [hep-ph].
[71] D. Alva, T. Han and R. Ruiz, "Heavy Majorana neutrinos from the $W\gamma$ fusion at hadron colliders", J. High Energy Phys. **02** (2015) 072.
[72] C. F. von Weizsacker, "Radiation emitted in collisions of very fast electrons," Z. Phys. **88**, 612 (1934).
[73] E. J. Williams,"Nature of the high-energy particles of penetrating radiation and status of ionization and radiation formulae," Phys. Rev. **45**, 729 (1934).
[74] J. J. Sakurai and D. Schildknecht, "Generalized vector dominance and inelastic electron - proton scattering," Phys. Lett. B **40**, 121 (1972).
[75] H. Terazawa, "Two photon processes for particle production at high-energies," Rev. Mod. Phys. **45**, 615 (1973).
[76] V. M. Budnev, I. F. Ginzburg, G. V. Meledin and V. G. Serbo,"The process p p $\to$ p p e^+ e^- and the possibility of its calculation by means of quantum electrodynamics only," Nucl. Phys. B **63**, 519 (1973).
[77] V. M. Budnev, I. F. Ginzburg, G. V. Meledin and V. G. Serbo, "The Two photon particle production mechanism. Physical problems. Applications. Equivalent photon approximation," Phys. Rept. **15**, 181 (1975).
[78] M. S. Chen, I. J. Muzinich, H. Terazawa and T. P. Cheng, "Lepton pair production from two-photon processes," Phys. Rev. D **7**, 3485 (1973).
[79] S. Chatrchyan *et al.* [CMS Collaboration], "Exclusive photon-photon production of muon pairs in proton-proton collisions at $\sqrt{s} = 7$ TeV," JHEP **1201**, 052 (2012)
[80] G. Aad *et al.* [ATLAS Collaboration], "Measurement of exclusive $\gamma\gamma \to \ell^+\ell^-$ production in proton-proton collisions at $\sqrt{s} = 7$ TeV with the ATLAS detector," arXiv:1506.07098 [hep-ex].
[81] T. Sjostrand, S. Mrenna, P. Z. Skands, J. High Energy Phys. 0605 (2006) 026, arXiv: hep-ph/0603175.
[82] S. Ovyn, X. Rouby, V. Lemaitre, arXiv: 0903.2225 [hep-ph].
[83] J. de Favereau, *et al.*, DELPHES 3 Collaboration, J. High Energy Phys. 1402 (2014) 057, arXiv: 1307.6346 [hep-ex].
[84] M. Cacciari, G. P. Salam, G. Soyez, J. High Energy Phys. 0804 (2008) 063, arXiv: 0802.1189 [hep-ph].
[85] M. Cacciari, G. P. Salam, G. Soyez, Eur. Phys. J. C 72 (2012) 1896, arXiv: 1111.6097 [hep-ph].
[86] R. D. Ball *et al.* [NNPDF Collaboration], "Parton distributions with QED corrections," Nucl. Phys. B **877**, 290 (2013) [arXiv:1308.0598 [hep-ph]].
[87] S. Carrazza [NNPDF Collaboration], "Towards the determination of the photon parton distribution func-

tion constrained by LHC data," PoS DIS **2013**, 279 (2013) [arXiv:1307.1131 [hep-ph]].
[88] S. Carrazza [NNPDF Collaboration], "Towards an unbiased determination of parton distributions with QED corrections," arXiv:1305.4179 [hep-ph].
[89] R. D. Ball *et al.* [NNPDF Collaboration], "Parton distributions for the LHC Run II," arXiv:1410.8849 [hep-ph].
[90] J. Pumplin, D. R. Stump, J. Huston, H. L. Lai, P. M. Nadolsky, W. K. Tung, J. High Energy Phys. 0207 (2002) 012, arXiv: hep-ph/0201195.